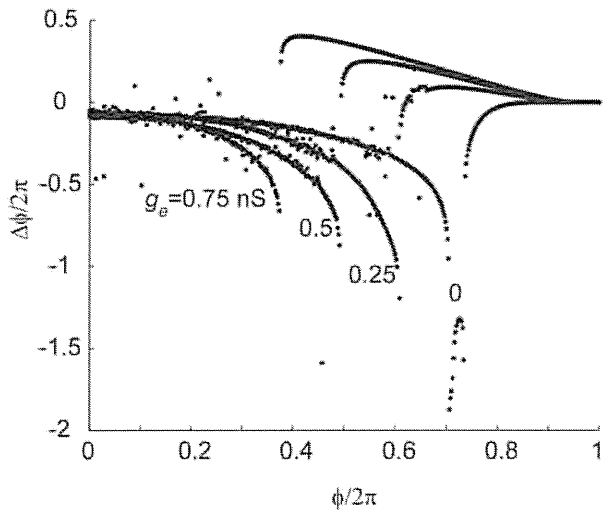

Figure 7. SPRF simulated for the Erisir *et al.*, 1999, fully-deterministic biophysical model of an FS cell. g_i=1.5 nS. 4 different values of g_e are used as indicated. F=40 Hz. Phase shifts are evaluated in steps of 0.002/2π in the onset phase of the compound synaptic input. Extraneous points lying off the main curves, particular for phase delays, reflect a complex local fine structure of the phase shift, around the central relationship.
doi:10.1371/journal.pcbi.1000951.g007

junctional input did affect phase delay strongly early in the cycle – this was never observed experimentally. This deficiency of the biophysical model suggests that additional conductances expressed in FS neurons somehow help to confer a complete immunity to gap-junctional stimulation in the early, phase-delay part of the cycle. We surmise that the voltage-gated potassium conductance in this part of the cycle may actually be much higher than in the model, and that this may allow phase delay and advance to be regulated completely independently. Also, because of their relative timing, the effect of inhibition will outlast that of the gap-junctional current transient – thus phase delays caused by inhibition starting early in the cycle may in fact be caused more by their persistence until later in the cycle. In addition, the model shows a pronounced curvature in the phase delay region of the SPRF which was not noticeable in any experimental recordings. This might reflect the presence of other voltage-dependent conductances in real FS cells which effectively linearize this part of the relationship.

The sharp discontinuity between phase delay and advance which emerges at high synaptic strengths is a result of the particular intrinsic biophysical properties and the nature of the synaptic perturbation. It appears to be related to the "class 2" nature of the FS neuron threshold [16], and may be sensitively determined by the potassium conductance densities and kinetics [42,43]. It was not observed for example in a class 1 excitable Morris-Lecar model. The discontinuity is a critical decision point, or threshold, in the progression of the membrane potential towards spike initiation, at which hyperpolarization and depolarization both exert their maximal influence. The effect of this shape of SPRF is to ensure very rapid synchronization of the cell. Maximal phase shift occurs in the middle of the cycle when the phase difference is high - the postsynaptic cell either advances or delays its phase to achieve nearly immediate in-phase firing when detuning between pre- and postsynaptic cell is small. This extremely sharp midcycle transition is not observed in conventional phase-resetting relationships to weak brief inputs in these cells [37,44], and is a consequence of the integration of the strong compound input.

The piecewise nature of the SPRF, with the phase advance contributed exclusively by gap-junctional input, and the delay component contributed exclusively by chemical inhibition, mean that these two types of connection have complementary roles in synchronization: gap junctions are necessary to entrain the firing of the postsynaptic cell to a frequency higher than its preferred frequency, while inhibitory synapses are necessary to entrain firing to a frequency lower than the preferred frequency (as seen in Figures 5 and 6). This can be seen as follows. Let H be the phase difference between postsynaptic and presynaptic cells ($\phi_{post}-\phi_{pre}$). The change in H over one period of the input, i.e. from input i to input $i+1$, is: $H_{i+1}-H_i=2\pi(F/f-1)+\Delta\phi(H_i)$. Therefore, when entrainment is achieved, $H_{i+1}=H_i=H_\infty$, and so if $F>f$, then $\Delta\phi(H_\infty)>0$, and if $F<f$, then $\Delta\phi(H_\infty)<0$.

Using the SPRF to predict entrainment

Using the SPRF to model entrainment assumes that the effect of each stimulus in the train is the same as if it was applied in isolation. The success of the SPRF in predicting entrainment shown here demonstrates that it is at least a good approximation for this purpose, and that the arithmetic of adding effects of multiple sequential synaptic inputs behaves reasonably linearly. The SPRF assumes that the entire dynamical state of the neuron may be represented by just a single number at any time, the phase, which would imply that its dynamical state always lies on a limit cycle, along which it is kicked instantaneously forwards and backwards by the synaptic inputs. The complex dynamics of a real neuron containing a large number of different voltage-dependent conductances distributed in a complex morphology, and the strong and non-instantaneous nature of the perturbation mean that this is a considerable simplification of the reality. An indication of whether the phase approximation is reasonably valid, is to test whether there is any higher-order phase resetting, i.e. changes in the interspike interval *following* that during which the input is applied, or in subsequent intervals. When we analysed second order shifts, we found that they were sometimes detectable, but very small in relation to the first-order SPRF (See Figure S1), in line with the short memory of FS cells for input conductance fluctuations [17].

Physiological consequences of the synaptic phase-resetting function

FS cell firing is suspected to be directly and primarily responsible for producing gamma oscillations in the neocortex [6,7,8]. Different fine-scale subnetworks of mutually-exciting pyramidal cells in layers 2 or 3, which are driven by specific subsets of local layer 4 inputs, appear to interact with other such subnetworks via the inhibitory interneuron network [45]. Synchronization of FS cells, therefore, may be essential for linking responses of pyramidal cells very rapidly to specific features of the synaptic input, as hypothesized to occur in sensory "binding" [2]. We have shown that the effect of conductance inputs which realistically mimic single synaptic connections on the phase of FS firing is very powerful, and is capable of entraining the postsynaptic cell even against strong noise. The strikingly sharp discontinuity between phase delay and advance in the SPRF causes a very rapid jump to nearly in-phase firing.

The relative strengths of electrical and inhibitory components can vary greatly from connection to connection [12,13], and some pairs of FS cells connected by gap junctions can synchronize their firing, while others cannot [14]. The strengths of these

components will also vary dynamically. Electrical synapses can exhibit plasticity through G protein-coupled receptor activation, intracellular calcium and phosphorylation [46], and the GABAergic connections show strong short-term depression [12,13,14]. These effects presumably help to shape the spatiotemporal dynamics of synchronous firing. The model that we introduce here could easily accommodate independent plasticity rules for inhibition and gap junctions, by additional rules for modifying the slopes of the corresponding regions of the SPRF. In addition to such modulation, the $GABA_A$ receptor is also the target of many important neuroactive drugs, such as benzodiazepines, barbiturates and ethanol. These will be expected to influence the shape of the SPRF, and the synchronization behavior of FS cells in the gamma frequency range. The SPRF, therefore, may be a useful tool for characterizing the action of such compounds on pathological network states treated by such drugs.

Firing is considerably more variable *in vivo* than *in vitro* [47], and it is important to consider the consequences of the SPRF in strong noise. The stochastic bifurcation analysis that we carried out (Fig. 6) delineated a well-defined boundary between entraining and non-entraining frequencies, based on a qualitative change in the nature of the motion of the phase [32] (see Methods). The stronger the noise, the smaller the frequency region of stochastic entrainment – in line with intuition, noise acts to break down synchronization. The strength of the noise effect in controlling the boundary of the synchronized region is not symmetrical around F – thus noise can effectively shift, as well as shrink the synchronized frequency band.

In conclusion, the synaptic phase-resetting function of FS cells firing at gamma frequencies, as characterized here, is very well-suited to achieving rapid synchronization, and demonstrates complementary roles of the two types of synaptic connection in determining the frequency range of synchronization. It provides a simple yet surprisingly accurate model for predicting synchronization of these cells, and should be a useful component in network models aimed at understanding the complex spatiotemporal properties of locally-synchronized gamma-frequency firing in the cortex.

Methods

Slice preparation and electrophysiological recording

300 μm sagittal slices of somatosensory cortex were prepared from postnatal day 13–19 Wistar rats, using a vibratome (DSK Microslicer Zero 1, Dosaka EM, Kyoto), in chilled solution composed of (in mM): 125 NaCl, 25 $NaHCO_3$, 2.5 KCl, 1.25 NaH_2PO_4, 2 $CaCl_2$, 1 $MgCl_2$, and 25 glucose, oxygenated with 95% O_2, 5% CO_2 gas. Slices were then held at room temperature for at least 30 minutes before recording. The tissue was visualized with an Olympus BX50WI upright microscope (Olympus UK, London) using infrared differential interference contrast videomicroscopy. During recording, slices were perfused with oxygenated solution identical to the slicing solution, at 31–35°C (8 cells analysed in detail) or 23°C (4 cells). 10 μM 2-(3-carboxypropyl)-3-amino-6-(4-methoxyphenyl)-pyridazinium bromide (SR95531; gabazine), 10 μM D-2-amino-5-phosphonopentanoic acid (AP5), and 10 μM 6-cyano-7-nitroquinoxaline-2,3-dione (CNQX) were usually added, to block chemical synaptic transmission mediated by $GABA_A$, N-methyl-D-aspartic acid (NMDA),and α-amino-3-hydroxy-5-methyl-4-isoxazole proprionic acid (AMPA) receptors, respectively. Whole-cell recordings were made from the somas of nonpyramidal neurons in cortical layers 2/3, 4, and 5. Cells identified as FS neurons had a mean input resistance of 202±87 MΩ ($n=12$). Data from 10 fast-spiking neurons (taken from 8 animals) were used for analysis, with a further 12 cells showing consistent results, but which were not complete enough for analysis. The number of synaptic phase-resetting functions with different parameters of the conductance perturbations (see below) which could be constructed for each cell was limited by the lifetime of the recording, typically 20 to 40 minutes.

Patch pipettes of 3–5 MΩ resistance were pulled from borosilicate capillary glass and filled with an intracellular solution containing (in mM): 105 K-gluconate, 30 KCl, 10 HEPES, 10 phosphocreatine, 4 ATP, 4 $MgCl_2$, and 0.3 GTP, adjusted to pH 7.3 with KOH. Current-clamp recordings were performed using an Axon Multiclamp 700A or in a few cases, an Axopatch 200A amplifier (Axon Instruments, Foster City, CA). Membrane potentials were corrected for nulling of the liquid junction potential before seal formation. Signals were filtered with a four-pole low-pass Bessel filter at −3dB cutoff frequency of 5 kHz, sampled at 20 kHz, and recorded with custom software written in MATLAB (The Mathworks, Natick, MA).

Conductance injection

Recorded neurons were stimulated using artificial conductance injection [25,26,48]. An effective conductance is inserted in the recorded cell by injecting a current I according to Ohm's law, $I=g(V-E_{rev})$, where g is the conductance, V is the membrane potential of the cell, and E_{rev} is the reversal potential of the conductance. A conductance injection amplifier [49] or digital signal processing system (SM-1 or SM-2, Cambridge Conductance, Cambridge, UK) [50] with response times of less than 200 ns or 10 μs respectively, were used to calculate and produce the current command signal in real time for the current-clamp amplifier.

Steady trains of action potentials at gamma frequencies were elicited by steps of AMPA-receptor like ohmic conductance, reversing at 0 mV, to which perturbing conductances were added as follows. Stimuli that mimicked action potentials filtered through electrical synapses were generated. An action potential (AP) waveform was produced using a conductance-based model of an FS cell, identical to that of [41], except that the leak conductance was reduced to better fit the stimulus-response curves of actual FS cells (see **Fast-spiking cell conductance-based model (section below)**

This AP waveform was then used as the time-varying E_{rev} signal for a constant conductance g_e, representing the electrical synapse. The conductance of a unitary synaptic GABA event was modelled as a difference of exponentials $g(t)=g_i[\exp(-t/\tau_2)-\exp(-t/\tau_1)]$, where g_i is the scaling amplitude of the inhibitory conductance, and τ_2 was 7 ms, and τ_1 was 0.5 ms. In compound stimuli, the start of the GABA event was delayed by 3 ms from the start of the simulated action potential to represent synaptic latency. The reversal potential E_{GABA} was usually set to −55 mV [29].

Data analysis

Spike times were determined as the times of positive-going threshold crossings of the membrane potential at a threshold set at 10 mV below the peak of action potentials. The phase at which a stimulus was applied was calculated from the time elapsed from the preceding spike, relative to the unperturbed firing period. Variability of phase was characterized by the phase order parameter, or synchrony $S=\sqrt{\langle\cos^2(\phi)\rangle+\langle\sin^2(\phi)\rangle}$, which varied between 0 (phases distributed uniformly between 0 and 2π) and 1 (phases all identical). The change in phase ($\Delta\phi$) caused by a stimulus was calculated as follows. Let ϕ be the phase reached at the moment of perturbation, ϕ' the phase immediately after, t_p the time after the *previous* spike at which the perturbation is applied, t_n the time elapsed after the perturbation before the *next* spike,

and T_0 the average interspike interval. Then $\phi=2\pi t_p/T_0$, $\phi'=2\pi(1-t_n/T_0)$ and $\Delta\phi=\phi'-\phi$.

Fitting and simulations

The synaptic phase-resetting function (SPRF, see Fig. 2) was approximated by the piecewise linear relationship:

$$\Delta\varphi(\varphi)=\begin{cases}-\alpha\varphi & (0\le\varphi<\varphi_c)\\ \beta(2\pi-\varphi) & (\varphi_c\le\varphi<2\pi)\end{cases} \quad (1)$$

where conductance values are in nS, -α is the slope in the phase advance section, -β is the slope of the phase delay section, and ϕ_c is the breakpoint. SPRFs were fitted to experiments by least-squares, and using Grubbs' test for outliers, to delete occasional outlying points (in most cases none, but no more than three per SPRF).

Entrainment of periodic spiking to periodic stimulation was simulated by the noisy map describing the evolution of the phase from stimulus n to stimulus $n+1$:

$$\varphi_{n+1}=G(\varphi_n)=\varphi_n+\Delta\varphi(\varphi_n)+2\pi F/f+\xi_n \pmod{2\pi} \quad (2)$$

where f is the stimulus angular frequency, F is the unperturbed (natural) angular frequency of the cell, and ξ_n is a Gaussian-distributed noise term, with variance σ^2. The biophysical simulations of Fig. 7 were carried out using the model specified by [41], modified slightly as described above (see **Conductance injection**).

Bifurcation analysis

Bifurcation points, where 1:1 entrained fixed points of the map given by Eq. 2 appear, were solved for directly. To determine the points of *stochastic* bifurcation, we used the definition of [32]. The stochastic map of the phase between successive stimuli on a unit circle S is represented by a Markov operator p on the phase distribution, where $p(\phi|\phi_0)$ is the conditional probability density function of the phase at stimulus $i+1$, given a phase of ϕ_0 at stimulus i.

$$p(\varphi|\varphi_0)=\frac{1}{\sqrt{2\pi\sigma}}\exp\left(\frac{(\varphi-G(\varphi_0))^2}{\sigma^2}\right) \pmod{2\pi},$$

and the distribution of phase $h(\phi)$ advances from stimulus n to stimulus $n+1$ according to:

$$h_{n+1}(\varphi)=\int_S p(\varphi|\varphi_0)h_n(\varphi)d\varphi_0 \pmod{2\pi}.$$

p is approximated by a stochastic transition matrix, and the onset of stochastic entrainment is defined by the point where the second eigenvalue of this stochastic transition matrix changes from real to complex. This definition of a stochastic bifurcation coincides with the deterministic case as the noise level approaches zero, is clearly defined even when the steady-state phase distribution hardly changes, and incorporates the dynamics of the phase: the first eigenfunction gives the stationary or invariant distribution of the phase, while the second eigenfunction can be thought of as forming the principal component of the average time course of relaxations from an initial random phase distribution.

Fast-spiking cell conductance-based model

A model of fast-spiking cell membrane potential (V) dynamics was used (as above for generating action potentials for gap-junctional stimulation) which was slightly modified, with a different leak conductance, from that specified in Erisir et al., 1999 [41] (also correcting typographical errors in the published description of the model). Sodium (Na), Kv1 (K1) and Kv3 type potassium and static leak (L) conductances were used in a single electrical compartment of capacitance C, as follows (units of mV for voltage, ms^{-1} for rates):

$$\frac{dV}{dt}=\frac{\bar{g}_{Na}m^3h(E_{Na}-V)+(\bar{g}_{K1}n^4+\bar{g}_{K3}p^2)(E_K-V)+g_L(E_L-V)}{C}$$

$$\frac{dx}{dt}=\alpha_x(V)(1-x)-\beta_x(V)x, \text{ for } x\in\{m,h,n,p\}, \text{ where}$$

$$\alpha_m(V)=(3020-40V)/(\exp((-75.5+V)/-13.5)-1),$$

$$\beta_m=1.2262/\exp(V/42.248)$$

$$\alpha_h(V)=0.0035/\exp(V/24.186),$$

$$\beta_h(V)=-(0.8712+0.017V)/(\exp((51.25+V)/-5.2)-1)$$

$$\alpha_n(V)=-(0.616+0.014V)/(\exp((44+V)/-2.3)-1),$$

$$\beta_n(V)=0.0043/\exp((44+V)/34)$$

$$\alpha_p(V)=(95-V)/(\exp((-95+V)/-11.8)-1),$$

$$\beta_p(V)=0.025/\exp(V/22.222)$$

$$C=8.04 \text{ pF}, \bar{g}_{Na}=900 \text{ nS}, \bar{g}_{K1}=1.8 \text{ nS}, \bar{g}_{K3}=1800 \text{ nS},$$

$$g_L=4.1 \text{ nS}, E_L=-70 \text{ mV}, E_K=-90 \text{ mV}, E_{Na}=60 \text{ mV}.$$

Exactly the same conductance stimuli were applied to the model as to cells experimentally (see **Conductance injection** section above).

Supporting Information

Figure S1 An example of the lack of phase shift in the cycle following that in which a strong perturbation is applied (second-order resetting). $F=61$ Hz, $g_e=0.4$ nS, $g_i=2$ nS. Dashed lines indicate expected standard deviation if there is no second order effect.
Found at: doi:10.1371/journal.pcbi.1000951.s001 (0.09 MB TIF)

Author Contributions

Conceived and designed the experiments: NWG TT KA HPCR. Performed the experiments: NWG HZ. Analyzed the data: NWG HZ KT HPCR. Wrote the paper: HPCR.

References

1. Buszaki G, Draguhn A (2004) Neuronal oscillations in cortical networks. Science 304: 1926–1929.
2. Singer W (1999) Neuronal synchrony: a versatile code for the definition of relations? Neuron 24: 49–65.
3. Fisahn A, Pike FG, Buhl EH, Paulsen O (1998) Cholinergic induction of network oscillations at 40 Hz in the hippocampus in vitro. Nature 394: 186–189.
4. Whittington MA, Traub RD, Jefferys JG (1995) Synchronized oscillations in interneuron networks driven by metabotropic glutamate receptor activation. Nature 373: 612–615.
5. Whittington MA, Stanford IM, Colling SB, Jefferys JG, Traub RD (1997) Spatiotemporal patterns of gamma frequency oscillations tetanically induced in the rat hippocampal slice. J Physiol 502(Pt 3): 591–607.

6. Cardin JA, Carlen M, Meletis K, Knoblich U, Zhang F, et al. (2009) Driving fast-spiking cells induces gamma rhythm and controls sensory responses. Nature 459: 663–667.
7. Hasenstaub A, Shu Y, Haider B, Kraushaar U, Duque A, et al. (2005) Inhibitory postsynaptic potentials carry synchronized frequency information in active cortical networks. Neuron 47: 423–435.
8. Morita K, Kalra R, Aihara K, Robinson HPC (2008) Recurrent Synaptic Input and the Timing of Gamma-Frequency-Modulated Firing of Pyramidal Cells during Neocortical "UP" States. J Neurosci 28: 1871–1881.
9. Lytton WW, Sejnowski TJ (1991) Simulations of cortical pyramidal neurons synchronized by inhibitory interneurons. J Neurophysiol 66: 1059–1079.
10. Vida I, Bartos M, Jonas P (2006) Shunting inhibition improves robustness of gamma oscillations in hippocampal interneuron networks by homogenizing firing rates. Neuron 49: 107–117.
11. White JA, Chow CC, Ritt J, Solo-Trevino C, Kopell N (1998) Synchronization and oscillatory dynamics in heterogeneous, mutually inhibited neurons. J Comput Neurosci 5: 5–16.
12. Galarreta M, Hestrin S (1999) A network of fast-spiking cells in the neocortex connected by electrical synapses. Nature 402: 72–75.
13. Gibson JR, Beierlein M, Connors BW (1999) Two networks of electrically coupled inhibitory neurons in neocortex. Nature 402: 75–79.
14. Tamas G, Buhl EH, Lorinz A, Somogyi P (2000) Proximally targeted GABAergic synapses and gap junctions synchronize cortical interneurons. Nat Neurosci 3: 366–371.
15. Bacci A, Huguenard JR (2006) Enhancement of spike-timing precision by autaptic transmission in neocortical inhibitory interneurons. Neuron 49: 118–130.
16. Tateno T, Harsch A, Robinson HP (2004) Threshold firing frequency-current relationships of neurons in rat somatosensory cortex: type 1 and type 2 dynamics. J Neurophysiol 92: 2283–2294.
17. Tateno T, Robinson HPC (2008) Integration of broadband conductance input in rat somatosensory cortical inhibitory interneurons: an inhibition-controlled switch between intrinsic and input-driven spiking in fast-spiking cells. J Neurophysiol 101: 1056–1072.
18. Traub RD (2001) Gap junctions between interneuron dendrites can enhance synchrony of gamma oscillations in distributed networks. J Neurosci 21: 9478–9486.
19. Bartos M (2002) Fast synaptic inhibition promotes synchronized gamma oscillations in hippocampal interneuron networks. Proc Natl Acad Sci U S A 99: 13222–13227.
20. Kopell N, Ermentrout GB (2004) Chemical and electrical synapses perform complementary roles in the synchronization of interneuronal networks. Proc Natl Acad Sci U S A 101: 15482–15487.
21. Rinzel JM, Ermentrout GB (1998) Analysis of neuronal excitability. In: CK, Segev I, eds. Methods in Neuronal Modelling. Cambridge MA: MIT Press.
22. Pikovsky A, Rosenblum M, Kurths J (2001) Synchronization: a universal concept in nonlinear sciences. Cambridge: Cambridge University Press.
23. Kawaguchi Y, Kubota Y (1993) Correlation of physiological subgroupings of nonpyramidal cells with parvalbumin- and calbindinD28k-immunoreactive neurons in layer V of rat frontal cortex. J Neurophysiol 70: 387–396.
24. Kawaguchi Y, Kubota Y (1997) GABAergic cell subtypes and their synaptic connections in rat frontal cortex. Cereb Cortex 7: 476–486.
25. Robinson HPC, Kawai N (1993) Injection of digitally synthesized synaptic conductance transients to measure the integrative properties of neurons. J Neurosci Methods 49: 157–165.
26. Sharp AA, O'Neil MB, Abbott LF, Marder E (1993) Dynamic clamp: computer-generated conductances in real neurons. J Neurophysiol 69: 992–995.
27. Amitai Y, Gibson JR, Beierlein M, Patrick SL, Ho AM, et al. (2002) The spatial dimensions of electrically coupled networks of interneurons in the neocortex. J Neurosci 22: 4142–4152.
28. Galarreta M, Hestrin S (2001) Electrical synapses between GABA-releasing interneurons. Nature Rev Neurosci 2: 425–433.
29. Martina M, Royer S, Pare D (2001) Cell-type-specific GABA responses and chloride homeostasis in the cortex and amygdala. J Neurophysiol 86: 2887–2895.
30. Gulledge AT, Stuart GJ (2003) Excitatory actions of GABA in the cortex. Neuron 37: 299–309.
31. Di Bernardo M, Budd CJ, Champneys AR (2001) Grazing and border-collision in piecewise-smooth systems: a unified analytical framework. Phys Rev Lett 86: 2553–2556.
32. Inoue J, Doi S, Kumagai S (2001) Numerical analysis of spectra of the Frobenius-Perron operator of a noisy one-dimensional mapping: Toward a theory of stochastic bifurcations. Phys Rev E Stat Nonlin Soft Matter Phys 64: 056219.
33. Ermentrout GB, Kopell N (1991) Multiple pulse interactions and averaging in systems of coupled neural oscillators. J Math Biology 29: 195–217.
34. Reyes AD, Fetz EE (1993) Two modes of interspike interval shortening by brief transient depolarizations in cat neocortical neurons. J Neurophysiol 69: 1661–1672.
35. Stoop R, Schindler K, Bunimovich LA (2000) When pyramidal neurons lock, when they respond chaotically, and when they like to synchronize. Neurosci Res 36: 81–91.
36. Netoff TI, Banks MI, Dorval AD, Acker CD, Haas JS, et al. (2005) Synchronization in hybrid neuronal networks of the hippocampal formation. J Neurophysiol 93: 1197–1208.
37. Mancilla JG, Lewis TJ, Pinto DJ, Rinzel J, Connors BW (2007) Synchronization of electrically coupled pairs of inhibitory interneurons in neocortex. J Neurosci 27: 2058–2073.
38. Hu H, Martina M, Jonas P (2009) Dendritic mechanisms underlying rapid synaptic activation of fast-spiking hippocampal interneurons. Science 327: 52–58.
39. Martina M, Vida I, Jonas P (2000) Distal initiation and active propagation of action potentials in interneuron dendrites. Science 287: 295–300.
40. Galarreta M, Hestrin S (2002) Electrical and chemical synapses among parvalbumin fast-spiking GABAergic interneurons in adult mouse neocortex. Proc Natl Acad Sci U S A 99: 12438–12443.
41. Erisir A, Lau D, Rudy B, Leonard CS (1999) Function of specific K(+) channels in sustained high-frequency firing of fast-spiking neocortical interneurons. J Neurophysiol 82: 2476–2489.
42. Gutkin BS, Ermentrout GB, Reyes AD (2005) Phase-response curves give the responses of neurons to transient inputs. J Neurophysiol 94: 1623–1635.
43. Ermentrout B, Wechselberger M (2009) Canards, clusters and synchronization in a weakly coupled interneuron model. SIAM J Applied Dynamical Systems 8: 253–278.
44. Tateno T, Robinson HP (2007) Phase resetting curves and oscillatory stability in interneurons of rat somatosensory cortex. Biophys J 92: 683–695.
45. Yoshimura Y, Callaway EM (2005) Fine-scale specificity of cortical networks depends on inhibitory cell type and connectivity. Nat Neurosci 8: 1552–1559.
46. Bennett MV, Zukin RS (2004) Electrical coupling and neuronal synchronization in the Mammalian brain. Neuron 41: 495–511.
47. Holt GR, Softky WR, Koch C, Douglas RJ (1996) Comparison of discharge variability in vitro and in vivo in cat visual cortex neurons. J Neurophysiol 75: 1806–1814.
48. Destexhe A, Bal T, eds (2009) Dynamic-Clamp: From Principles to Applications: Springer.
49. Robinson HPC (1998) Analog circuits for injecting time-varying linear and nonlinear (NMDA-type) conductances into neurons. J Physiol 518P: 9–10.
50. Robinson HPC (2008) A scriptable DSP-based system for dynamic conductance injection. J Neurosci Methods 169: 271–281.

A small-conductance Ca^{2+}-dependent K^+ current regulates dopamine neuron activity: a combined approach of dynamic current clamping and intracellular imaging of calcium signals

Takashi Tateno

To analyze the small-conductance calcium-dependent K^+ current observed in dopaminergic neurons of the rat midbrain, we have developed a new dynamic current clamping method that incorporates recording of intracellular Ca^{2+} levels. As reported earlier, blocking the small-conductance current with apamin shifted the firing modes of dopaminergic neurons and changed the firing rate and spike afterhyperpolarization. We modeled the kinetic properties of the current and assessed the model in a real-time computational system. Here, we show that the spike afterhyperpolarization is regulated by the small-conductance current, an effect that is observed in dopaminergic neurons. Thus, this current can effectively shape the autonomous firing patterns of dopaminergic neurons. *NeuroReport* **21:667–674 © 2010 Wolters Kluwer Health | Lippincott Williams & Wilkins.**

NeuroReport 2010, 21:667–674

Keywords: action potential, dynamic clamp, intracellular calcium, rat midbrain, spike after hyperpolarization, whole-cell patch-clamp recording

Osaka University, Toyonaka-shi, Osaka, Japan

Correspondence to Dr Takashi Tateno, PhD, PRESTO, Japan Science and Technology Agency, 4-1-8 Honcho, Kawaguchi, Saitama, Japan

Present address: Takashi Tateno, Department of Mechanical Science and Bioengineering, Graduate School of Engineering Science, Osaka University, 1-3, Machikaneyama, Toyonaka, Osaka, 560-8531 Japan

Received 3 April 2010 **accepted** 11 April 2010

Introduction

Dopaminergic (DA) neurons are integral to a wide variety of behaviors, including reward-based learning [1], cognition [2], and motor control [3]. Although recent studies have provided significant insights into the properties of ion channels in in-vitro preparations [4], the roles of distinct ion channels in controlling the frequency and regularity of the various discharge modes of DA midbrain neurons have not yet been systematically studied in awake, behaving animals. Several types of Ca^{2+} channels – for example, L-type, N-type, P/Q-type, and T-type channels – are expressed in DA neurons [5,6]. $Ca_V1.3$ L-type channels [7–9] are important for autonomous firing of DA neurons, where they activate at relatively negative potentials compared with the $Ca_V1.2$ channels [10]. Subthreshold activation of T-type and N-type Ca^{2+} channels results in the activation of an apamin-sensitive small-conductance (SK)-mediated current, which contributes medium afterhyperpolarization [11–13]. The medium afterhyperpolarization activates rapidly and decays over several hundred milliseconds, whereas slow afterhyperpolarizations, which can typically last over several hundred milliseconds to several seconds [14], are coupled to P-type and L-type Ca^{2+} channels [15] as well as SK channels. The blockade of this SK current leads to long-duration, Ca^{2+}-dependent plateau potentials [12,16].

Since its introduction [17,18], the dynamic clamp technique has slowly become a standard technique for performing cellular electrophysiological analysis. The dynamic clamp involves injecting conductance into an intracellularly recorded cell. As the current is the product of the conductance and the membrane potential, which itself changes as current is injected, the injected current must be continuously updated as a function of the membrane potential of the recorded cell. Therefore, a real-time loop needs to be established between the device that produces the current and the recorded membrane potential. The applications of this technique have expanded from studies of single neuron properties [19] to the creation of hybrid networks that combine biological and simulated neurons [20]. Despite the wealth of physiological and pathophysiological information about the role of the intracellular calcium concentration $[Ca^{2+}]_i$ in neuronal functions, however, no attempts to link the measured $[Ca^{2+}]_i$ to a dynamic clamp recording directly have been reported to date. In this study, we propose a new dynamic clamp technique in which the $[Ca^{2+}]_i$ measured using fluorescence imaging is incorporated into the conventional dynamic clamp protocol. Here, we report that the frequency of action potentials in the midbrain DA neurons is profoundly influenced by the SK Ca^{2+}-dependent K^+ current. We also use the new method to inject an artificial SK current and characterize the effects on DA neuron activity.

Methods

Slice preparation

Slices of the basal ganglia were obtained from P15–P18 Wistar rats. The animals were anesthetized and decapitated.

Supplemental digital content is available for this article. Direct URL citations appear in the printed text and are provided in the HTML and PDF versions of this article on the journal's Website (*www.neuroreport.com*).

0959-4965 © 2010 Wolters Kluwer Health | Lippincott Williams & Wilkins

DOI: 10.1097/WNR.0b013e32833add56

The brain was placed in artificial cerebral spinal fluid (ACSF) consisting of 125 mM NaCl, 2.5 mM KCl, 25 mM $NaHCO_2$, 25 mM glucose, 1.25 mM NaH_2PO_4, 2 mM $CaCl_2$, and 1 mM $MgCl_2$, in which bubbles of 95% O_2/5% CO_2 were used to obtain a pH of 7.4. The basal ganglia were mounted on a vibratome and cut into 300-μm-thick coronal slices. The slices, including the substantia nigra pars compacta (SNc) and the lateral part of the ventral tegmental area (VTA), were incubated in ACSF at 32°C for at least 1 h before recording. All procedures were approved by Osaka University and complied with the NIH Guidelines on Animal Use.

Electrophysiology

Basal ganglia slices were placed in a recording chamber perfused with ACSF containing 100 μM picrotoxin or 10 μM gabazine (Sigma-Aldrich; St Louis, Missouri, USA), 10 μM CNQX, and 10 μM AP5 (Tocris Cookson, Bristol, UK) to prevent synaptic transmission. The samples were maintained at 34 ± 2°C. The slices were visualized using an Olympus BW60WI microscope and DA neurons in the SNc and the lateral part of the VTA were identified using a 60 × water immersion objective lens. All the recorded neurons were subjected to immunocytochemical detection of tyrosine hydroxylase to confirm that they were DA neurons. Glass pipette electrodes were pulled from borosilicate glass (Clark GC150F-5) and were filled with an intracellular solution consisting of 105 mM K gluconate, 30 mM KCl, 10 mM HEPES, 10 mM phosphocreatine Na_2, 4 mM ATP-Mg, 0.3 mM Na-GTP, and 5 mg/ml biocytin (adjusted to pH 7.3 using KOH). Whole-cell patch clamp recordings were made using a Multiclamp 700B amplifier (Molecular Devices, Sunnyvale, California, USA). To block the SK current, 10–100 nM apamin (Sigma-Aldrich) was added to the perfusion solution. Current clamp recordings were sampled at 20 kHz using an NI PCI-6259 DAQ card (National Instruments, Austin, Texas, USA) and custom data acquisition software written in MATLAB (Mathworks, Natick, Massachusetts, USA).

Ca^{2+} imaging

Ratiometric and single-wavelength measurements of fluorescence at 340 and/or 380 nm were made using a fluorescence microscopy camera, EXi blue (Q Imaging, Surrey, British Columbia, Canada), and a dye fura-2 (Molecular Probes, Eugene, Oregon, USA). Frame rates of 50–80 per second were used, depending on the size of the field of view. The measurements were made at the position in which the main proximal dendrite connected to the soma of the DA neuron. For each trial, fluorescence values at 340 and 380 nm were first converted to the calcium concentration at rest as described earlier [21], whereas, in some experiments, the membrane was hyperpolarized to prevent oscillations in the current clamp mode. Subsequent changes in fluorescence at 380 nm were then converted into $[Ca^{2+}]_i$ using a formula that was reported earlier (see also Appendix A in the Supplemental digital information, Supplemental digital content 1, *http://links.lww.com/WNR/A56*) [22]. Calculation of the $[Ca^{2+}]_i$ was carried out in real time using a digital signal processor (sBOX, MTT, Tokyo, Japan). The fura-2 concentration in the cell was assumed to be 0 μM just before the electrode broke into the cell and 100 μM (concentration in the electrode) at steady state. The concentration at any time could then be extrapolated from the filling curve described by Foehring *et al.* [23].

Dynamic current clamp

The dynamic current clamp was used to produce artificial SK conductance in DA neurons after apamin treatment. As SK conductance is calcium-dependent, we had to measure the $[Ca^{2+}]_i$ directly, or simulate a calcium pool and calcium flow into this pool in real time based on the voltage trajectory of the recorded neuron. For the latter, the calcium inflow in our model was mediated by L-type, N-type, P-type, and T-type voltage-dependent calcium currents that were simulated using Hodgkin–Huxley kinetics and were linked in real time to the recorded voltage (see Appendix B in the Supplemental digital information, Supplemental digital content 1, *http://links.lww.com/WNR/A56*). In the model, we selected types of voltage-dependent calcium currents and their kinetics on the basis of a series of DA neuron models proposed by Canavier *et al.* [24,25]. Some parameters in the model were modified by using data of recent studies ([5]; see also Appendix B in the Supplemental digital information, Supplemental digital content 1, *http://links.lww.com/WNR/A56*). Calcium outflow governed the signal decay and the SK current was determined using the Hill equation-based calcium-binding activation and the time course of the measured or simulated $[Ca^{2+}]_i$. The equations used (in the dynamic clamp are listed in the Supplemental digital information, Supplemental digital content 1, *http://links.lww.com/WNR/A56*) and were implemented in the digital signal processor with custom-made programs written using Code Composer Studio 3.1 (Texas Instruments, Dallas, Texas, USA).

The results are reported as mean ± SD. Statistical analysis was performed using Student's *t*-test, and *P* value of less than 0.05 was considered to be significant.

Results

We recorded and imaged 48 DA neurons in the SNc and eight DA neurons in the lateral part of the VTA (total 37 animals). Each of the DA neurons showed spontaneous firing at 1.97 ± 0.23 Hz (mean ± SD). In some experiments, the membrane was hyperpolarized before obtaining evoked responses to prevent oscillations in the current clamp mode (see Methods section). We obtained a membrane voltage trace based on an injected current step pulse (100 pA) before and after the application of 20 or 100 nM apamin (Fig. 1A). For nine and eight DA

Fig. 1

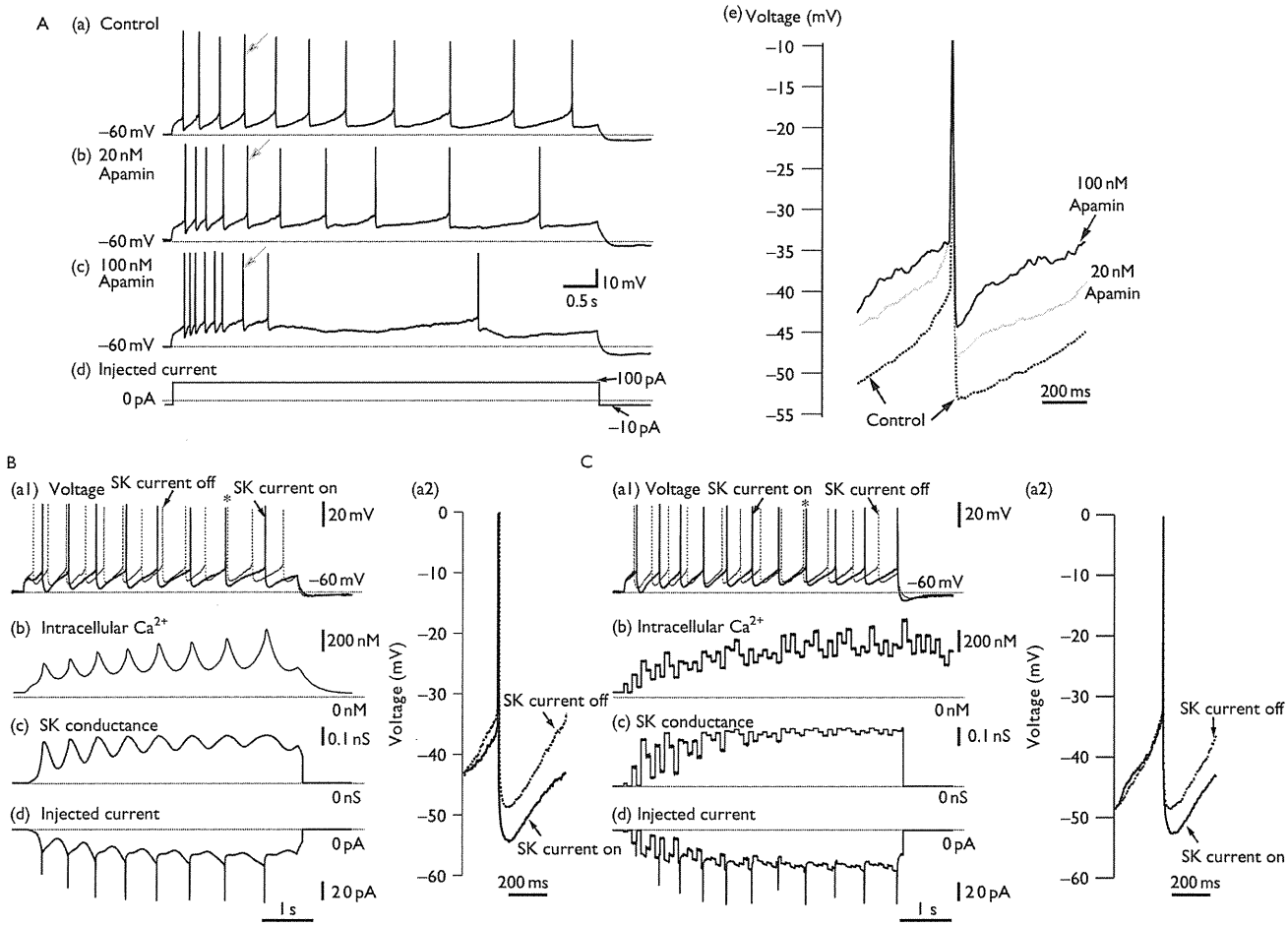

A, Apamin effects on the firing properties of a dopaminergic (DA) neuron. In response to a current step of 100 pA from −10 pA, repetitive firing was observed in (a) control, (b) 20 nM apamin, and (c) 100 nM apamin conditions. The injected current is shown in (d). In (e), an expanded view of the action potentials indicated by arrows in (a), (b), and (c) and the afterhyperpolarizations (AHPs) are shown. B, In the presence of 20 nM apamin, injection of small-conductance (SK) current simulated from the recorded membrane voltage mimicked and restored AHP waveforms. Results are shown for the (a) membrane voltage, (b) $[Ca^{2+}]_i$ computed from a mathematical model that incorporated the recorded voltage, (c) the SK value, and (d) the injected SK current. In (a2), an expanded view of the action potentials indicated by an asterisk in (a1) and the AHPs are shown. C, Similar traces to those shown in B, except that the $[Ca^{2+}]_i$ was estimated using fluorescence imaging.

neurons in the SNc and the lateral part of the VTA, respectively, irregular bursting appeared in the presence of 100 nM apamin [Fig. 1A(c)], whereas regular single spiking was evoked in control samples or in neurons treated with less than 30 nM apamin. In 100 nM apamin, the negative voltage peak following each spike increased (-45.4 ± 1.9 vs. -53.7 ± 0.68 mV in control samples, $P < 0.001$), such that the afterhyperpolarization (AHP) was smaller. In other words, if the AHP was smaller, the minimum membrane potential reached was less negative, so that it increased in the presence of apamin, as shown in Fig. 1A(e). In addition, the peak amplitude of each spike was reduced (12.3 ± 0.8 vs. 14.4 ± 0.7 mV in control samples, $P < 0.01$).

In the presence of 20 nM apamin, the artificial SK current injection rescued the AHP or the minimum membrane potential reached, and the negative voltage peak after each spike was reduced and more hyperpolarized, so that the minimum membrane potentials decreased (-58.3 ± 2.5 mV); the negative peak value without the SK current was -52.8 ± 3.1 mV [Fig. 1B(a) and C(a)]. Moreover, the simulated and measured $[Ca^{2+}]_i$ is also shown in Fig. 1B(b) and C(b), respectively. The average changes in the transient $[Ca^{2+}]_i$ estimated using fluorescence imaging were similar to those observed for the transient $[Ca^{2+}]_i$ simulated using the recorded membrane voltage. Owing to a limited time resolution, however, fine oscillatory changes during evoked responses were not easily observed using the present imaging system [Fig. 2C(b)].

On the bases of the changes in the $[Ca^{2+}]_i$, the SK conductance was directly calculated using a Hill equation-based calcium-binding activation formula (Hill coefficient

Fig. 2

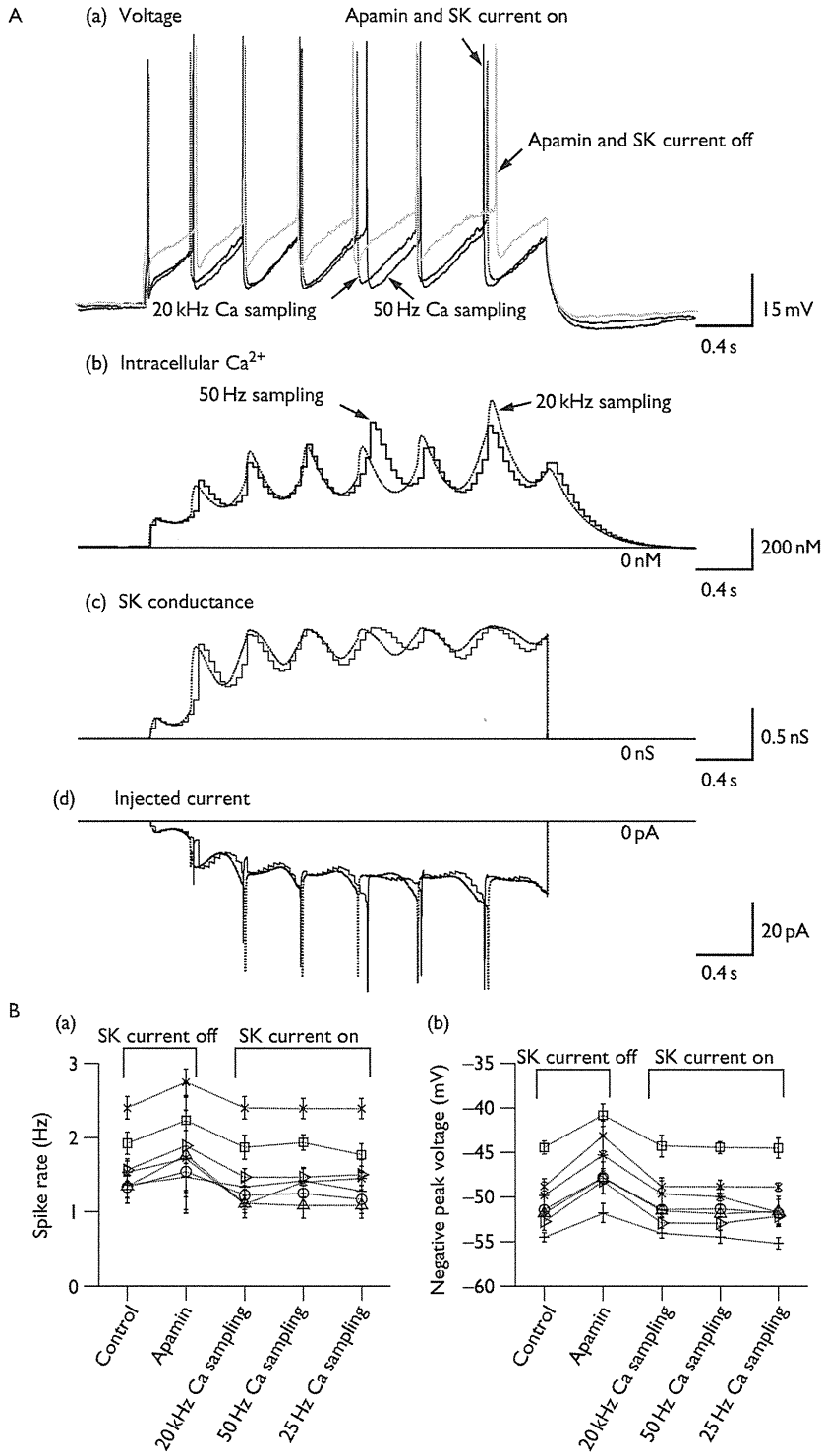

A, (a) Effects of different sampling rates in the calcium dynamics model on the firing properties of a dopaminergic (DA) neuron. In response to a current step of 100 pA from −10 pA, repetitive firing was observed before and after small-conductance (SK) current was injected while the endogenous SK current was blocked (30 nM apamin treatment). Results at 20 kHz and 50 Hz Ca sampling are shown for the (a) membrane voltage, (b) $[Ca^{2+}]_i$ computed from a mathematical model that incorporated the recorded voltage, (c) the SK value, and (d) the injected SK current. (b) Spike statistics at three different sampling rates (20 000, 50, and 25 Hz) in the calcium dynamics model for three and four DA neurons in the substantia nigra pars compacta and the ventral tegmental area, respectively. B, Results of spike rate in (a) and negative peak voltage following each spike in (b) are shown in a control condition before SK current was injected and 30 nM apamin treatment conditions before and after SK current was injected. Error bars indicate standard deviations.

$n = 4$): $\bar{g}_{SK}([Ca^{2+}]_i) = \bar{g}_{SK}[Ca^{2+}]_i^4/([Ca^{2+}]_i^4 + K_m^4)$, where $\bar{g}_{SK}$ and K_m are the maximum SK value and dissociation constant, respectively [Fig. 1B(c) and C(c)]. Moreover, in the presence of apamin, the dynamic clamp stimulated a pulsatile SK current in each spike with a subsequent slow transient [Fig. 1B(d) and C(d)]. For the SK value obtained using fluorescence imaging of $[Ca^{2+}]_i$ changes, the oscillatory phase observed in Fig. 1C(d) was not easily identified, although the observed trend was similar to that simulated using the computational model [Fig. 1B(d)]. The decay time for the SK current was dominated by the time courses of the membrane voltage changes between spikes and calcium outflow during the early phase of the evoked responses. During the late phase, the time course of the membrane voltage changes mediated the fast transient because of calcium accumulation.

In our imaging system, it was impossible to increase the imaging rate (e.g. > 80 frames/s) for the intracellular Ca^{2+} measurements sufficiently to test the model in which the recorded membrane voltage was sampled at 20 kHz. Therefore, to test the calcium dynamics model, we used a lower resolution at a sampling rate of less than 50 Hz, which was comparable to that of the fluorescence data. In the calcium dynamics model at sampling rates of 20 kHz and 50 Hz, Fig. 2A(a)–(d) shows four traces of membrane voltage, simulated $[Ca^{2+}]_i$, SK conductance, and an injected current, respectively. Between the two sampling rates, for three and four DA neurons in the SNc and VTA, respectively, there were no significant differences in the average spike rate and the negative peak voltage following each spike or AHP, as shown in Fig. 2B(a) and (b).

From the result mentioned above, the sampling rates in the calcium dynamics model had little influence on the spike rate and AHP of DA neurons. Thus, the model is valid for replacing $[Ca^{2+}]_i$ measured by calcium imaging with the computed $[Ca^{2+}]_i$. In the following, therefore, SK conductance was generated from the model of calcium dynamics.

All the neurons recorded in this study showed altered spontaneous firing properties after SK current block with 100 nM apamin (Fig. 3B), compared with the baseline activity (Fig. 3A). After apamin treatment, the AHP disappeared or was reduced (i.e. the minimum membrane potential reached was increased) during both spontaneous firing and evoked responses. In the presence or absence of apamin, the negative peak amplitude after each spike was -62.3 ± 1.2 mV ($\bar{g}_{SK} = 200$ nS) or -57.6 ± 1.5 mV ($\bar{g}_{SK} = 0$), respectively. Elimination of the AHP with apamin led to pronounced burst activity in most neurons (Fig. 3B). In those neurons, interspike intervals (ISIs; 0.31 ± 0.25 s) during the burst were shorter than baseline ISIs (0.71 ± 0.11 s), and the number of spikes in each burst varied [Fig. 3B(b)].

Fig. 3

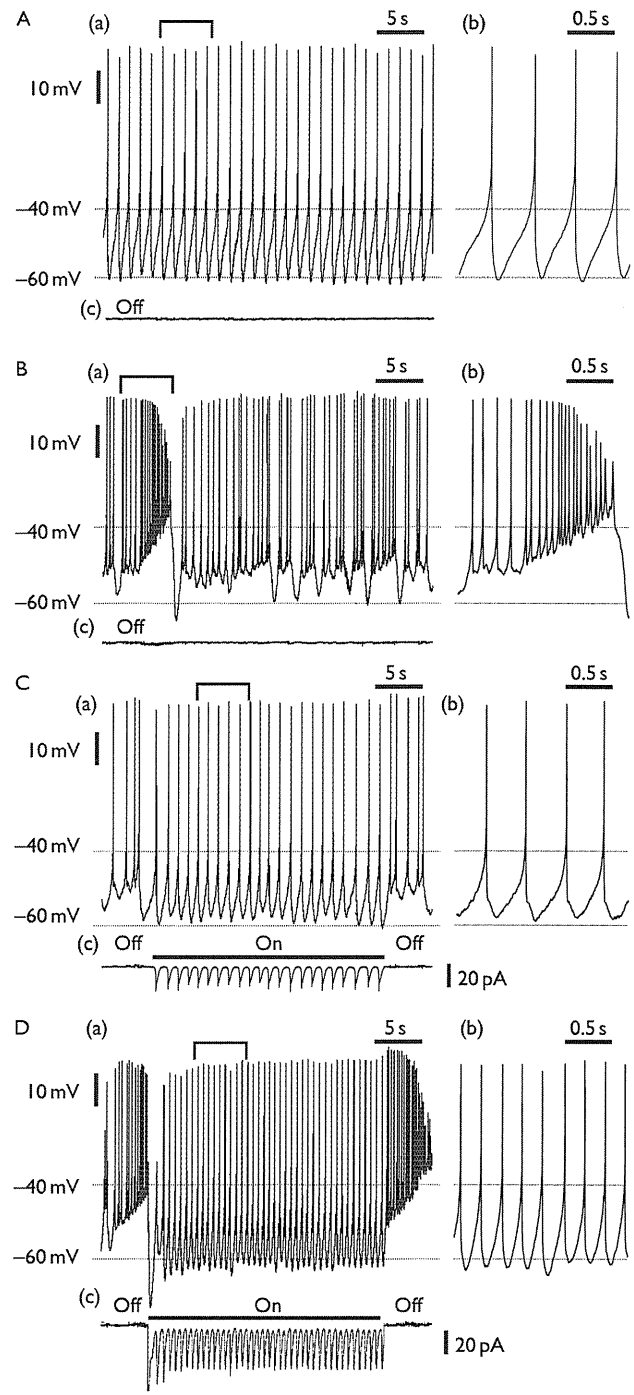

Spontaneous spiking activity in control samples, samples treated with apamin, and in the presence of injected small-conductance (SK) current. A, (a) Baseline spiking at 2.1 Hz in a dopaminergic (DA) neuron. (b) The afterhyperpolarization (AHP) between spikes. B, (a) Bursting behavior in the presence of 100 nM apamin. (b) The AHP was absent and spike rate increased during each burst. C, (a) An artificial SK current prevented bursting and regular firing was observed. (b) The AHP recovered to the level shown in A. D, When bursting increased, more artificial SK current was needed to restore baseline activity with a faster spiking rate of 3.6 Hz and a deeper AHP.

To restore baseline spiking while the endogenous SK current was blocked with apamin, we adjusted the parameters that described the artificial SK current applied with dynamic clamping (see Methods section). Figure 3C shows that the artificial SK current (20–50 pA) restored regular single spiking. Further, when the current injection was removed, irregular bursting reappeared immediately.

In control and SK current injection conditions [Fig. 4A(a) and (b), respectively], positive correlations were observed between the negative peak after each spike and the spontaneous spike rate of the DA neurons. This indicates that spike frequency was controlled by the SK current, as reported by Feng and Jaeger [26] for neurons of deep cerebellar nuclei. Figure 4A(c) shows that, in some DA neurons (eight of 12 cells), an artificial SK current injection slightly increased spontaneous firing. This observation may be related to the fact that the restored negative peak voltage after spikes was slightly higher than that observed without the SK current injection.

The recovery of regular spiking in the presence of apamin depended on both the extent of irregular bursting and the injected SK current. As shown in Fig. 3D, longer periods of bursting required an SK current between 50 and 100 pA. In all of the tested cases ($n = 12$), the application of the artificial SK current during an apamin-induced bursting led to regular spiking. Therefore, the coefficients of variation of the ISIs in the presence of apamin were reduced to the control level (0.1–0.2) if the SK conductance was adjusted to an appropriate cell-specific value. Figure 4B shows that single-spike activity and regularity recovered when the SK values were adjusted.

A calcium concentration decay time constant between 20 and 35 ms was able to restore the time course of the AHPs. Decays in the calcium levels have been directly measured after evoking single spikes in response to a briefly (30–50 ms) injected step current. The average value of the decay time constant was 34.3 ± 8.0 ms ($n = 5$) immediately after the cell membrane was broken. Therefore, the result was consistent with those obtained in the SK current injection experiments, although the measured average value was slightly larger than that used in the model.

Discussion

Here, we reported a new dynamic clamp technique in which Ca^{2+} levels were used to adjust a conventional dynamic clamp protocol. With the technique, we estimated the injected SK current from both directly measured Ca^{2+}-derived fluorescence signals and a mathematical model of intracellular Ca^{2+} dynamics. This approach enabled us to test our mathematical models in real time by observing the neurons' firing modes and spike properties.

Fig. 4

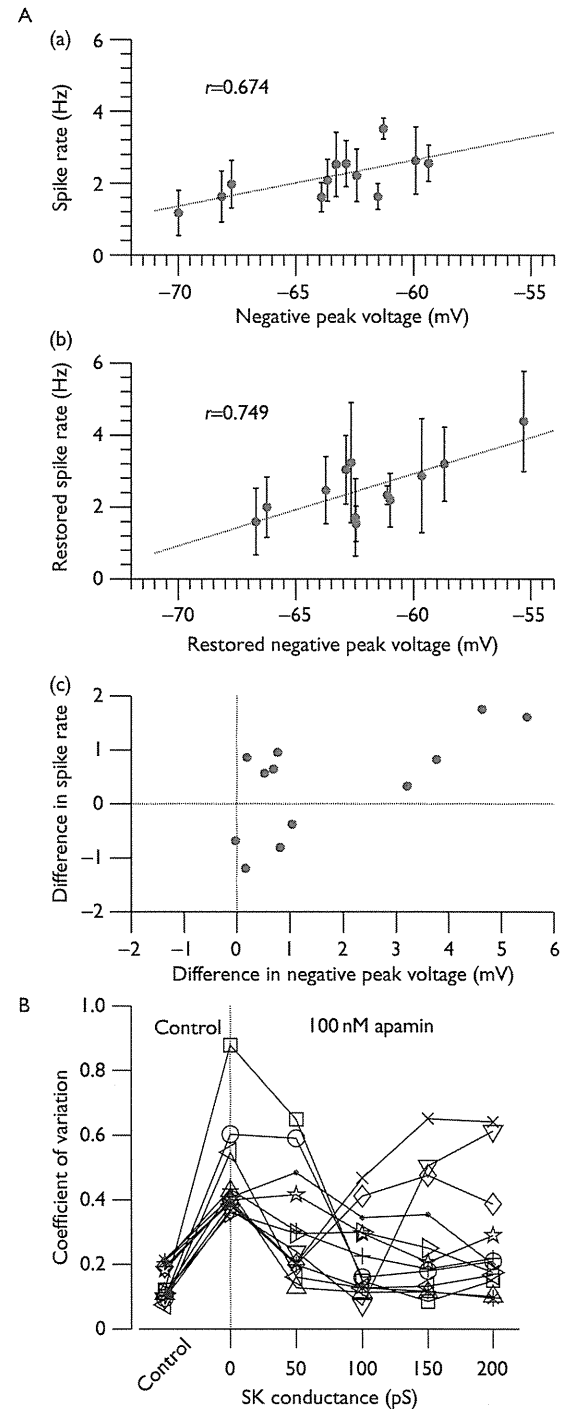

A, (a) Spike statistics before and after small-conductance (SK) current was injected while the endogenous SK current was blocked. Positive correlations were observed between the negative peak voltages after spikes and the spontaneous firing rate (a) before SK current block and (b) after an artificial SK current was injected. The correlation coefficients (r) are indicated. (c) The relationships between the original and the recovered negative peak voltages and the firing rate are shown ($n = 12$ cells). B, Variable or consistent spiking in control samples, or in the presence or absence of injected SK current. Coefficients of variation (SD/mean) for the interspike intervals are plotted.

DA neurons showed several typical firing modes *in vivo*, including burst activity and low-frequency tonic firing (< 10 Hz) with regular or irregular patterns. In contrast, DA cells *in vitro* fire autonomously and tonically with a regular pattern. The calcium current that mediates the autonomous regular firing is likely, at least partly carried by L-type Ca^{2+} channels, because it is inhibited by L-type channel blockers, but not N-type channel blockers [6,9,15]. Although the effects of P/Q-type channel blockers on this activity have not yet been determined *in vivo*, Puopolo *et al.* [15] showed that a selective P-type channel blocker markedly inhibited firing in the midbrain slices. Treatment of DA neurons in these brain slice preparations with apamin shifted the firing mode from a regular firing pattern to a burst pattern. In DA cells, therefore, the firing mode and action potential frequency and initiation are regulated by an SK Ca^{2+}-dependent K^+ current.

We showed that the SK current in DA neurons partly accounts for the AHP and contributes to the regularity of the ISIs. Our results also showed that, in response to the current injection under baseline conditions, the AHP is the predominant regulator of the spike frequency. A recent study showed that the SK current in DA neurons is primarily the result of inflow through T-type and N-type channels together with minor contributions from several other calcium currents [13]. In this study, we applied an artificial SK current with dynamic clamping using four types of Ca^{2+} current as the calcium source. The results revealed that pulsatile calcium inflow after each spike and subsequent calcium decay with a time constant ranging from 20 to 35 ms could explain the observed AHP properties. As indicated in other studies [26], the decay of the intracellular calcium pool may represent the short period of time for which the SK channels are exposed to an elevated calcium concentration at the membrane. Thus, the short exposure may allow intracellular calcium to accumulate without elevation of the SK current.

The minimum artificial SK current amplitude that was required to eliminate irregular and burst spiking was such that the ensuing AHP had a slightly larger amplitude than that recorded during the baseline activity. This, however, did not necessarily slow the recovery of regular spiking compared with the pre-apamin treatment condition. Rather, at times, it accelerated regular spontaneous firing in the tested DA neurons [Fig. 3A(c)]. This observation may be associated with the rapid recovery of a spike refractory period, which always occurred when the inhibitory synaptic input was injected. We showed that certain SK values promoted regular ISIs in the DA neurons. This value needed to be adjusted to restore regular tonic firing in the presence of apamin, because the appropriate value was cell specific. Although the maximum injected current amplitude was 50 pA, the time course of the injected current was critical to control the firing mode.

Calcium signals generated by voltage-dependent Ca^{2+} channels may be amplified by secondary calcium release from intracellular stores, which has also been shown to activate SK channels. Indeed, SK channels in the DA neurons can be activated by the intracellular calcium release evoked through metabotropic glutamate receptors [27]. This secondary calcium release may contribute to the discrepancy observed in the latter portions of the $[Ca^{2+}]_i$ time courses obtained using Ca^{2+}-derived fluorescence signals and numerical simulation with our model [see Fig. 1B(b) and C(b)].

Recent studies have shown that the midbrain DA neurons are a heterogeneous population of neurons and that there is a media-lateral gradient in SK3 channel expression [28]. However, in the presence of apamin, we could not find any differences between the recorded DA neurons in the SNc and those in the lateral part of the VTA. The reason for this may be that the number of sampled VTA DA neurons was small (eight cells) and they were located in the lateral part of the VTA in which the SK3 channels are highly expressed [28].

Ji and Shepard [29] reported that local and systemic administration of apamin increases the incidence and intensity of the bursting activity among the DA neurons recorded in intact rats. However, they also pointed out that, consistent with its effects in brain slices, the ability of apamin to increase bursting activity *in vivo* could not have been simply presupposed. Pacemaker activity exhibited by the DA neurons *in vitro* or pacing with a scale of high precision such that the coefficient of variation in the interspike intervals is less than 12%, is rarely observed *in vivo*, where the continuum of the patterned activity is often attributed to synaptic inputs. Therefore, in addition to the mechanism involving SK channels, DA cells also require *N*-methyl-D-aspartate (NMDA) receptor-gated channels for burst activity. Under certain in-vivo conditions, either or both of these mechanisms could induce burst firing. NMDA receptor-mediated burst firing would be induced by inputs from glutamate-containing synaptic connections. The approach presented here may help elucidate these mechanisms, because the dynamic clamp technique can be used to mimic NMDA-like synaptic inputs.

Conclusion

To test the validity of a Ca^{2+}-dependent K^+ current model in in-vitro preparations of DA neurons in the SNc and the lateral part of the VTA, we developed a new dynamic clamp technique in which fluorescence imaging of Ca^{2+} levels was incorporated into a conventional dynamic clamp protocol. As reported before, our experimental results combined with mathematical modeling indicate that an SK Ca^{2+}-dependent K^+ current markedly shapes the firing modes and spike properties of these neurons. In addition, our results support the fact that the

measurement of intracellular Ca^{2+} level can be possibly replaced with the calcium dynamics model as an input to the dynamic clamp system.

Acknowledgements

Grant support: Precursory research for Embryonic Science and Technology (PRESTO), Japan Science and Technology Agency (JST). Grant-in-Aid for Scientific Research (B) and Exploratory Research, the Ministry of Education, Culture, Sports, Science and Technology (MEXT).

References

1 Schultz W. Getting formal with dopamine and reward. *Neuron* 2002; **36**:241–263.
2 Brozoski TJ, Brown RM, Rosvold HE, Goldman PS. Cognitive deficit caused by regional depletion of dopamine in prefrontal cortex of rhesus monkey. *Science* 1979; **205**:929–932.
3 Graybiel AM, Aosaki T, Flaherty AW, Kimura M. The basal ganglia and adaptive motor control. *Science* 1994; **265**:1826–1831.
4 Liss B, Roeper J. Individual dopamine midbrain neurons: functional diversity and flexibility in health and disease. *Brain Res Rev* 2008; **58**:314–321.
5 Durante P, Cardenas CG, Whittaker JA, Kitai ST, Scroggs RS. Low-threshold L-type calcium channels in rat dopamine neurons. *J Neurophysiol* 2004; **91**:1450–1454.
6 Nedergaard S, Flatman JA, Engberg I. Nifedipine- and omega-conotoxin-sensitive Ca^{2+} conductances in guinea-pig substantia nigra pars compacta neurones. *J Physiol* 1993; **466**:727–747.
7 Chan CS, Guzman JN, Ilijic E, Mercer JN, Rick C, Tkatch T, *et al.* Rejuvenation protects neurons in mouse models of Parkinson's disease. *Nature* 2007; **447**:1081–1086.
8 Kang Y, Kitai ST. A whole cell patch-clamp study on the pacemaker potential in dopaminergic neurons of rat substantia nigra compacta. *Neurosci Res* 1993; **18**:209–221.
9 Mercuri NB, Bonci A, Calabresi P, Stratta F, Stefani A, Bernardi G. Effects of dihydropyridine calcium antagonists on rat midbrain dopaminergic neurones. *Br J Pharmacol* 1994; **113**:831–838.
10 Xu W, Lipscombe D. Neuronal Ca(V)1.3alpha(1) L-type channels activate at relatively hyperpolarized membrane potentials and are incompletely inhibited by dihydropyridines. *J Neurosci* 2001; **21**:5944–5951.
11 Ping HX, Shepard PD. Apamin-sensitive Ca(2+)-activated K+ channels regulate pacemaker activity in nigral dopamine neurons. *Neuroreport* 1996; **7**:809–814.
12 Shepard PD, Bunney BS. Repetitive firing properties of putative dopamine-containing neurons in vitro: regulation by an apamin-sensitive Ca(2+)-activated K+ conductance. *Exp Brain Res* 1991; **86**:141–150.
13 Wolfart J, Roeper J. Selective coupling of T-type calcium channels to SK potassium channels prevents intrinsic bursting in dopaminergic midbrain neurons. *J Neurosci* 2002; **22**:3404–3413.
14 Faber ESL. Functions and modulation of neuronal SK channels. *Cell Biochem Biophys* 2009; **55**:127–139.
15 Puopolo M, Raviola E, Bean BP. Roles of subthreshold calcium current and sodium current in spontaneous firing of mouse midbrain dopamine neurons. *J Neurosci* 2007; **27**:645–656.
16 Johnson SW, Wu YN. Multiple mechanisms underlie burst firing in rat midbrain dopamine neurons in vitro. *Brain Res* 2004; **1019**:293–296.
17 Robinson HP, Kawai N. Injection of digitally synthesized synaptic conductance transients to measure the integrative properties of neurons. *J Neurosci Methods* 1993; **49**:157–165.
18 Sharp AA, O'Neil MB, Abbott LF, Marder E. Dynamic clamp: computer-generated conductances in real neurons. *J Neurophysiol* 1993; **69**:992–995.
19 Destexhe A, Rudolph M, Fellous JM, Sejnowski TJ. Fluctuating synaptic conductances recreate in vivo-like activity in neocortical neurons. *Neuroscience* 2001; **107**:13–24.
20 Sieling FH, Canavier CC, Prinz AA. Predictions of phase-locking in excitatory hybrid networks: excitation does not promote phase-locking in pattern-generating networks as reliably as inhibition. *J Neurophysiol* 2009; **102**:69–84.
21 Grynkiewicz G, Poenie M, Tsien RY. A new generation of Ca^{2+} indicators with greatly improved fluorescence properties. *J Biol Chem* 1985; **260**:3440–3450.
22 Wilson CJ, Callaway JC. Coupled oscillator model of the dopaminergic neuron of the substantia nigra. *J Neurophysiol* 2000; **83**:3084–3100.
23 Foehring RC, Zhang XF, Lee JC, Callaway JC. Endogenous calcium buffering capacity of substantia nigral dopamine neurons. *J Neurophysiol* 2009; **102**:2326–2333.
24 Amini B, Clark JW Jr, Canavier CC. Calcium dynamics underlying pacemaker-like and burst firing oscillations in midbrain dopaminergic neurons: a computational study. *J Neurophysiol* 1999; **82**:2249–2261.
25 Canavier CC, Oprisan SA, Callaway JC, Ji H, Shepard PD. Computational model predicts a role for ERG current in repolarizing plateau potentials in dopamine neurons: implications for modulation of neuronal activity. *J Neurophysiol* 2007; **98**:3006–3022.
26 Feng SS, Jaeger D. The role of SK calcium-dependent potassium currents in regulating the activity of deep cerebellar nucleus neurons: a dynamic clamp study. *Cerebellum* 2008; **7**:542–546.
27 Morikawa H, Imani F, Khodakhah K, Williams JT. Inositol 1,4,5-triphosphate-evoked responses in midbrain dopamine neurons. *J Neurosci* 2000; **20**:RC103.
28 Sarpal D, Koenig JI, Adelman JP, Brady D, Prendeville LC, Shepard PD. Regional distribution of SK3 mRNA-containing neurons in the adult and adolescent rat ventral midbrain and their relationship to dopamine-containing cells. *Synapse* 2004; **53**:104–113.
29 Ji H, Shepard PD. SK Ca^{2+}-activated K^+ channel ligands alter the firing pattern of dopamine-containing neurons in vivo. *Neuroscience* 2006; **140**:623–633.

Sensors and Actuators A 158 (2010) 183–192

Contents lists available at ScienceDirect

Sensors and Actuators A: Physical

journal homepage: www.elsevier.com/locate/sna

Development of piezoelectric acoustic sensor with frequency selectivity for artificial cochlea

Hirofumi Shintaku[a,*], Takayuki Nakagawa[b], Dai Kitagawa[a], Harto Tanujaya[a], Satoyuki Kawano[a], Juichi Ito[b]

[a] *Department of Mechanical Science and Bioengineering, Graduate School of Engineering Science, Osaka University, Machikaneyama-cho 1-3, Toyonaka, Osaka 560-8531, Japan*
[b] *Department of Otolaryngology, Head and Neck Surgery, Graduate School of Medicine, Kyoto University, Kawahara-cho 54,Shogoin, Sakyo-ku, Kyoto 606-8507, Japan*

ARTICLE INFO

Article history:
Received 25 July 2009
Received in revised form
13 November 2009
Accepted 22 December 2009
Available online 4 January 2010

Keywords:
Fluid-structure interaction
Acoustic MEMS sensor
Artificial cochlea
Biomechanical engineering
Piezoelectric device

ABSTRACT

In this paper, we report a novel piezoelectric artificial cochlea which realizes both acoustic/electric conversion and frequency selectivity without an external energy supply. The device comprises an artificial basilar membrane (ABM) which is made of a 40 μm thick polyvinylidine difluoride (PVDF) membrane fixed on a substrate with a trapezoidal slit. The ABM over the slit, which mimics the biological system, is vibrated by acoustic waves and generates electric output due to the piezoelectric effect of PVDF. The width of ABM is linearly varied from 2.0 to 4.0 mm along the longitudinal direction of 30 mm to change its local resonant frequency with respect to the position. A detecting electrode array with 24-elements of 0.50 × 1.0 mm rectangles is made of an aluminum thin film on ABM, where they are located in a center line of longitudinal direction with the gaps of 0.50 mm. Since the device will be implanted into a cochlea filled with lymph fluid in future, the basic characteristics in terms of vibration and acoustic/electric conversion are investigated both in the air and in the silicone oil which is a model of lymph fluid. The in vitro optical measurements show that the local resonant frequency of vibration is varied along the longitudinal direction from 6.6 to 19.8 kHz in the air and from 1.4 to 4.9 kHz in the silicone oil, respectively. Since a resonating place vibrates with relatively large amplitude, the electric output there becomes high and that at the other electrodes remains to be low. Thus, the electric voltages from each electrode realize the frequency selectivity. Furthermore, the effect of surrounding fluid on the vibration is discussed in detail by comparing the experimental results with the theoretical predictions obtained by the Wentzel–Kramers–Brillouin asymptotic method. The theoretical prediction indicates that the surrounding fluid of the higher density induces the larger effective mass for the vibration that results in lower resonant frequency. From these findings, the feasibility of artificial cochlea is confirmed both experimentally and theoretically.

1. Introduction

The sensorineural hearing loss is a type of deafness which is often caused by the damage on hair cells of cochleae in inner ears. The hair cells convert acoustic sounds to electric signals that stimulate auditory nerves. As a clinical treatment for the hearing loss in children and adults, the artificial cochlea is recently well used. The device bypasses the damaged hair cells by generating the electric current in response to the acoustic sound [1,2]. The current artificial cochlea consists of an implantable electrode array for the stimulation and an extracorporeal device including a microphone, a sound processor and a battery. The acoustic sound is detected and is analyzed with respect to the frequency by the extracorporeal device. The processed signals are transferred through a transcutaneous system. Then, the auditory nerves are stimulated through the electrodes inserted in the cochlea. The disadvantages in the current system are the indispensability of extracorporeal devices, the small number of electrodes which closely connects to the limitation of tones, and the relatively large power consumption. This situation motivates us to develop a fully self-contained implantable artificial cochlea.

The important functions of cochlea are not only the conversion of acoustic wave to electric signals but also the frequency selectivity [3,4]. The basilar membrane which is a biological diaphragm in the cochlea plays an important role for the frequency selectivity. The local eigen frequency of membrane is changing along the place

* Corresponding author. Tel.: +81 6 6850 6179; fax: +81 6 6850 6179.
E-mail address: shintaku@me.es.osaka-u.ac.jp (H. Shintaku).

0924-4247/$ – see front matter © 2009 Elsevier B.V. All rights reserved.
doi:10.1016/j.sna.2009.12.021

Nomenclature

A_j	Fourier coefficient
$b(x)$	width of ABM, m
D	bending rigidity, N m
E	Young's modulus, Pa
f	frequency, Hz
h	thickness of ABM, m
$k(x)$	wave number, m^{-1}
L_1	width of fluid channel, m
L_2	depth of fluid channel, m
L_3	length of ABM, m
p_f	pressure, Pa
w	displacement of ABM, m
$W(x)$	envelope function, m
(x, y, z)	Cartesian coordinates, m

Greek letters

$\eta(x, y)$	shape function for ABM's bending in y direction
ν	Poisson ratio
ρ_f	density of fluid, kg m^{-3}
ρ_m	density of PVDF, kg m^{-3}
$\phi_f(x, y, z, t)$	velocity potential, m^2/s
ω	angular frequency, rad/s

Subscripts

f	region of fluid channel f = l or u
j	mode number of Fourier coefficient
l	lower fluid channel
m	PVDF
u	upper fluid channel

of it, because of varying mechanical boundary conditions and the mechanical rigidity. Thus, when the eigen frequency at a local place match to that of acoustic wave, the place vibrates with relatively large amplitude due to the resonance. The vibration stimulates hair cells especially at the resonated place. As a result, the frequency of acoustic wave is recognized as the difference in tones.

To artificially realize the frequency selectivity, some microscaled devices have been reported. Tanaka et al. [5] and Xu et al. [6] developed acoustic sensors with the function of frequency selectivity by the use of resonance of cantilever arrays. Those sensors were evaluated in the atmospheric environment. Chen et al. [7] developed a beam array fixed on a trapezoidal channel and investigated the vibrating characteristics in the water. Despite the frequency selectivity of cantilevers or beams, their mechanical strength may not be enough for the implantation as the artificial cochleae for the long period. On the other hand, White and Grosh [8] developed a device made of polyimide membrane with Si_3N_4 beams. The demonstration for the frequency selectivity was conducted at the higher frequency range compared with the audible one. Wittbrodt et al. [9] also developed a device made of polyimide membrane with Al beams. They reported that the device possessed some similarities with the biological cochlea in terms of traveling waves, the frequency to place tonotopic organization, and the roll off beyond the characteristic place.

The acoustic sensor which is developed in this paper realizes both the frequency selectivity and the conversion of acoustic wave to the electric signal in the liquid environment without an external energy supply. The device is designed as a prototype model to test the basic concept of the acoustic sensor for the development of the self-contained implantable artificial cochlea. The device consists of a piezoelectric membrane fixed on a trapezoidal slit, where the membrane over the slit works as a detector. We name this trapezoidal membrane as an artificial basilar membrane (ABM). Discrete electrodes are fabricated on ABM by technologies of micro electromechanical systems (MEMS) to measure the electric signals generated in response to the externally applied acoustic waves. To model the liquid environment, the fluid channel which locates under ABM is filled with a silicone oil as a model of lymph fluid in the cochlea. The ABM's vibration is measured using a laser Doppler vibrometer (LDV) at the various frequencies in the range of 1.0–20 kHz. The electric output is measured through the electrodes using a preamplifier. To predict the performance of the present device, the oscillatory dynamics of ABM is theoretically analyzed based on the vibrating equation of a thin plate bending and equations for the fluid dynamics. The phenomenon of fluid-structure interaction is treated by coupling those basic equations. To treat the wave motion on trapezoidal ABM, the Wentzel–Kramers–Brillouin (WKB) asymptotic solution [10] is used under the assumption of the gradually varying wavelength. The comparison between the experimental and theoretical results makes clear the detailed mechanism underlying the frequency selectivity. In addition, discussions for the further development as an implantable artificial cochlea are described from the viewpoint of magnitude of electric signal and the device size.

2. Principles and experimental methods

2.1. Basic mechanism of frequency selectivity and electric signal generation

A schematic and a photograph of piezoelectric acoustic sensor developed here are shown in Fig. 1. The device comprises a polyvinylidine difluoride (PVDF) membrane (KUREHA, Japan) bonded on a stainless plate with a trapezoidal slit and discrete electrodes distributed along x axis. PVDF is a piezoelectric material which can convert mechanical stresses to electric signals. The trapezoidal slit is designed so that the membrane over it, i.e. ABM, can be easily vibrated by the acoustic wave. The width $b(x)$ of ABM is linearly varied in the ranges of 2.0–4.0 mm along x of 30 mm long. This shape is intended to mimic the passive basilar membrane, that is, the local resonant frequency (LRF) of ABM gradually changes due to the varying mechanical boundary conditions along x. LRF is expected to be decreased as x increases. Applying acoustic wave with a certain frequency to ABM, a local place vibrates with relatively large amplitude due to the resonance. Electric signals are generated by the piezoelectric effect with respect to the local stress in ABM. Thus, the electrode on the resonating place gives a relatively large electric output. This is the basic mechanism of frequency selectivity realized by the association of resonance of vibration and the discrete electrode array. The device is mounted on a substrate with a fluid channel, where the channel dimensions are 47 × 17 mm rectangle and 4 mm deep. To model an in vivo environment, the fluid channel is filled with silicone oil (Shin-Etsu Chemical, Japan). The density and the viscosity of silicone oil are 873 kg/m^3 and 1.75 × 10^{-3} Pa s, respectively, where those of lymph fluid in cochleae are typically reported as 1.0 × 10^3 kg/m^3 [11] and from 1.0 × 10^{-3} to 1.97 × 10^{-3} Pa s [12,13], respectively. Although the both sides of basilar membrane in vivo face to the lymph fluid, in this experiment, only the bottom side of ABM faces to the silicone oil for the stable optical measurement from the upper side. The effect of this simplification is discussed by the theoretical analysis in the later section. Furthermore, the size of this ABM is relatively large to be implanted into the human cochlea. However, the main purpose of this paper is to test the basic mechanism of proposed system in terms of acoustic/electric conversion and the frequency selectivity. The optimization and the miniaturization will be remained as a future work. The advantages of miniaturized ABM are again discussed in later section.

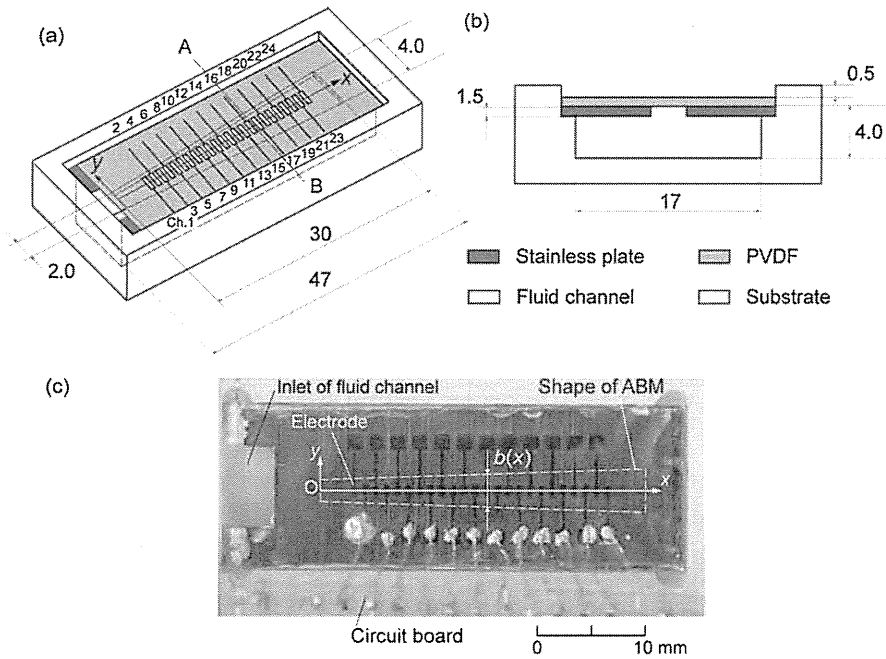

Fig. 1. Schematic and photograph of piezoelectric acoustic sensor; (a) 3D view, (b) cross sectional view at AB, and (c) photograph (Unit: mm).

2.2. Experimental setup

The electrode array with 24 elements made of an aluminum thin film is fabricated on an upper side of a 40 μm thick PVDF membrane based on a standard photolithography and an etching process. For convenience, the electrodes are named as Ch.1–Ch.24 as shown in Fig. 1(a). The each electrode of 0.50 × 1.0 mm rectangular shape is equally spaced 1.0 mm center to center, resulting in a gap of 0.50 mm between two adjacent electrodes. The ground electrode is prepared as a common one for all discrete electrodes on the lower side of ABM. The membrane is glued on the stainless plate to be the trapezoidal ABM. Since the electrodes of about 100 nm thick are extremely thinner than the PVDF of 40 μm, they may not strongly affect on the vibrating characteristics of ABM.

Fig. 2 shows a schematic of experimental setup. The sinusoidal acoustic wave is applied to the device from a speaker (FOSTEX, Japan) which is located 120 mm distant with 45° at a tilt. The speaker is previously calibrated to realize the constant sound pressure with the precision of ±0.1 dBSPL at various frequencies. The frequency is controlled by the function generator (NF, Japan) from 1.0 to 20 kHz which is in the range of audible frequency. The device on the substrate is set on a motorized stage which moves x and y directions for the measurement of spatial distribution of vibration amplitude. The velocity of ABM in z due to the vibration by the acoustic wave is measured by the LDV (Graphtec, Japan). The displacement, which is converted from the velocity data, is analyzed by an FFT to obtain the amplitude of vibration at the frequency of acoustic wave. At the same time, the piezoelectric output from the electrodes is measured in terms of voltage using a preamplifier and an oscilloscope.

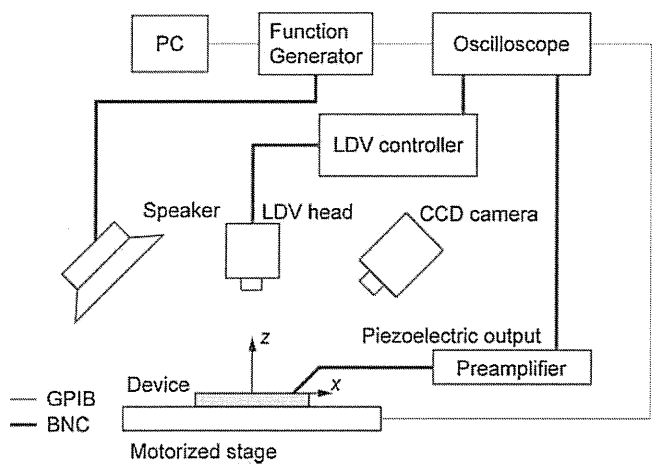

Fig. 2. Schematic of experimental setup for measurement of vibrating characteristics of ABM.

2.3. Oscillatory dynamics of artificial basilar membrane

Because the phenomena including the fluid-structure interaction are relatively complex, it is important for practical engineering to develop a theoretical model that effectively and easily predicts the vibrating characteristics of ABM. To obtain a mathematical solution, the following assumptions are made based on the experimental observations.

(1) The vibration of ABM is modeled as the bending vibration of a thin plate with small-amplitudes. The plain stress condition is valid, since the thickness h of ABM is small compared with the width or length.
(2) The fluid flow is assumed as incompressible, since $O(\omega^2 L^2/c^2)$ is 10^{-2}–10^{-6}, where the angular frequency ω is $O(10^3)$–$O(10^5)$, the characteristic length L is $O(10^{-3})$, and the sound velocity c is $O(10^3)$.
(3) The effects of gravity and viscosity of surrounding fluid are ignored.

The governing equation for the bending vibration of a plate with isotropic mechanical properties can be described as

$$\rho_m h \frac{\partial^2 w}{\partial t^2} + D\left[\frac{\partial^4 w}{\partial x^4} + 2\frac{\partial^4 w}{\partial x^2 \partial y^2} + \frac{\partial^4 w}{\partial y^4}\right] = p_0 \quad (1)$$

where D, p_0, w, and ρ_m are the bending rigidity, the pressure of acoustic wave, the displacement in z direction, and the density of ABM, respectively. The bending rigidity D is related to Young's modulus E as

$$D = \frac{Eh^3}{12(1-\nu^2)} \tag{2}$$

where ν is the Poisson ratio.

The basic equation for the fluid flow is the Laplace equation of velocity potential ϕ_f as

$$\frac{\partial^2\phi_f}{\partial x^2} + \frac{\partial^2\phi_f}{\partial y^2} + \frac{\partial^2\phi_f}{\partial z^2} = 0 \tag{3}$$

The velocity potential ϕ_f is related to the velocity components (u_x, u_y, u_z) as

$$u_x = \frac{\partial\phi_f}{\partial x}, \quad u_y = \frac{\partial\phi_f}{\partial y}, \quad u_z = \frac{\partial\phi_f}{\partial z} \tag{4}$$

respectively. The subscript f is u or l, where u and l indicate the fluid at the upper and lower sides of ABM, respectively. Furthermore, the velocity potential ϕ_f is related to the pressure as

$$\rho_f\frac{\partial\phi_f}{\partial t} = -p_f \tag{5}$$

where ρ_f is the density of fluid.

The governing equations are solved with the following boundary conditions. The normal velocities at the wall of fluid channel are written as

$$u_z = \frac{\partial\phi_l}{\partial z} = 0 \quad \text{at} \quad z = -L_2 \tag{6}$$

$$u_y = \frac{\partial\phi_l}{\partial y} = 0 \quad \text{at} \quad y = \pm\frac{L_1}{2} \tag{7}$$

where L_1 and L_2 are the width and the depth of fluid channel, respectively. The kinematic boundary condition at $z=0$ is written as

$$\frac{\partial w}{\partial t} = \frac{\partial\phi_f}{\partial z} \quad \text{at} \quad z = 0 \tag{8}$$

The thickness h of ABM is ignored in the analysis of fluid flow, since it is relatively small compared with the depth L_2 of fluid channel. The pressure p_0 is the pressure difference between the upper and lower sides of ABM and can be written as

$$p_0 = -\rho_l\frac{\partial\phi_l}{\partial t} + \rho_u\frac{\partial\phi_u}{\partial t} \quad \text{at} \quad z = 0 \tag{9}$$

Since ρ_l is extremely large compared with ρ_u in the present experiment, Eq. (9) is approximated as

$$p_0 \cong -\rho_l\frac{\partial\phi_l}{\partial t} \quad \text{at} \quad z = 0 \tag{10}$$

To obtain the oscillatory solution at the periodic steady state, following assumptions are made.

(4) A single mode $\eta(x, y)$ is used for the shape function of ABM's bending in y direction. $\eta(x,y)$ is determined based on the analytical solution of a vibrating beam with the first mode, the length of $b(x)$, and the fixed boundary conditions at $y=\pm b(x)/2$ as

$$\eta(x,y) = \begin{cases} c_1\cos\left(\dfrac{\beta}{b(x)}y\right) + c_2\cosh\left(\dfrac{\beta}{b(x)}y\right) & \text{at} \quad -\dfrac{b(x)}{2} \le y \le \dfrac{b(x)}{2} \\ 0 \quad \text{at} \quad -\dfrac{L_1}{2} \le y \le -\dfrac{b(x)}{2} \quad \text{and} \quad \dfrac{b(x)}{2} \le y \le \dfrac{L_1}{2} \end{cases} \tag{11}$$

where c_1, c_2, and β are constants of 0.8827, 0.1173 and 4.730, respectively. These constants are determined to make $\eta(x, y)$ satisfy the fixed boundary conditions at $y=\pm b(x)/2$.

(5) The wave is considered as a slowly varying wave in x direction. That is, the wave number $k(x)$ is slowly varying along x as $b(x)$, where $db(x)/dx \cong 0$ and $dk(x)/dx \cong 0$ are reasonable in the scale of a one wavelength. In this case, the waves can be treated as pseudo plane ones and can be described by the WKB asymptotic solution [10].

Based on these assumptions described above, the displacement $w(x, y, t)$ of ABM can be written as

$$w = W(x)\eta(x,y)e^{i\int_0^x k(\xi)d\xi}e^{-i\omega t} \tag{12}$$

where i and $W(x)$ are the imaginary number and the envelope function, respectively. $W(x)$ is also treated as a slowly varying function, that is $dW(x)/dx \cong 0$, since the effect of $dW(x)/dx$ on the dispersion relationship is trivial for linear problems [14]. The main purpose of the theoretical analysis is to predict the distribution of the local resonant frequency and to clarify the effect of the surrounding fluid on the resonance. Therefore, to simplify the mathematical development, only the forward wave is included in the analysis. On the other hand, the solution for Eq. (3) which satisfies the boundary conditions of Eqs. (6) and (7) is written as

$$\phi_l = \sum_{j=0}^{\infty} A_j\cosh\left[\zeta_j(z+L_2)\right]\cos\left(\frac{j\pi}{L_1}y\right)e^{i\int_0^x k(\xi)d\xi}e^{-i\omega t} \tag{13}$$

where A_j and ζ_j are the Fourier coefficient for jth mode and $[k^2(x)+(j\pi/L_1)^2]^{1/2}$, respectively. From Eqs. (8), (12) and (13), the following equation is obtained:

$$i\omega W(x)\eta(x,y) = -\sum_{j=0}^{\infty} A_j\zeta_j\sinh(\zeta_j L_2)\cos\left(\frac{j\pi}{L_1}y\right) \tag{14}$$

Using the orthogonality of cosine function, A_j is calculated as

$$A_j = -\frac{i\omega W(x)\int_{-b(x)/2}^{b(x)/2}\eta(x,y)\cos\left(j\pi y/L_1\right)dy}{\zeta_j\sinh\left(\zeta_j L_2\right)\int_{-L_1/2}^{L_1/2}\cos^2\left(j\pi y/L_1\right)dy} \tag{15}$$

Eqs. (10) and (12) are substituted into Eq. (1). Then, multiplying $\eta(x,y)$ to Eq. (1), and integrating from $-b(x)/2$ to $b(x)/2$ with respect to y, the following eikonal equation is obtained:

$$\begin{aligned} f(x,\omega) &= D\left[k^4(x)\int_{-b(x)/2}^{b(x)/2}\eta^2(x,y)dy - 2k^2(x)\right. \\ &\times\left.\int_{-b(x)/2}^{b(x)/2}\eta(x,y)\partial^2\eta(x,y)/\partial y^2 dy + \left[\beta/b(x)\right]^4\int_{-b(x)/2}^{b(x)/2}\eta^2(x,y)dy\right] \\ &-\omega^2\left[\rho_m h\int_{-b(x)/2}^{b(x)/2}\eta^2(x,y)dy + \rho_l\sum_{j=0}^{\infty}\frac{\left[\int_{-b(x)/2}^{b(x)/2}\eta(x,y)\cos\left(j\pi y/L_1\right)dy\right]^2}{\zeta_j\tanh\left(\zeta_j L_2\right)\int_{-L_1/2}^{L_1/2}\cos^2\left(j\pi y/L_1\right)dy}\right] \end{aligned} \tag{16}$$

Eq. (16) describes the dispersion relationship between $k(x)$ and ω at various x. The effect of surrounding fluid is found in the last term of Eq. (16). Since this term contributes to increase the effective mass for the vibration, the resonant frequency may be decreased by the surrounding fluid. From the average variation principle [14], it is known that the eikonal equation has the relationship with $W(x)$ as

$$W(x) = \frac{c}{\left(\frac{\partial f}{\partial k}\right)^{1/2}} \tag{17}$$

Table 1
Parameters for prediction.

Parameter	Symbol	Value
Width of ABM (m)	$b(x)$	$b(x)=0.002+0.002x/L_3$
Young's modulus of PVDF (Pa)	E	3×10^{9} [a]
Width of fluid channel (m)	L_1	0.017
Depth of fluid channel (m)	L_2	0.004
Length of ABM (m)	L_3	0.03
Poisson ratio of PVDF	ν	0.29[a]
Density of PVDF (kg/m^3)	ρ_m	1780 [15]
Density of silicone oil (kg/m^3)	ρ_s	873[b]
Density of air (kg/m^3)	ρ_a	1.2 [16]

[a] From technical report by KUREHA.
[b] From technical report by Shin-Etsu Chemical.

where c is a constant. Eq. (17) is the transport equation which describes the qualitative distribution of $W(x)$.

The parameters for the prediction are listed in Table 1. If the angular frequency ω is given as that of externally applied acoustic wave, only the wave number $k(x)$ is a variable to be solved in Eq. (16), where Eq. (16) is reduced to $f(k(x))=0$. At various ω, Eq. (16) is solved numerically by the Newton method. The iteration procedure is repeated until the residual becomes less than a specified tolerance of 10^{-6}. The term including summation is treated from $j=0$ to 30, which is adequate for the tolerance. The calculation is conducted for the two cases of filling the fluid channel with the air and of that with the liquid. The frequency is changed in the ranges of 3.5–14.0 kHz in the air environment and 0.7–3.6 kHz in the liquid environment, respectively. At those frequencies, Eq. (16) gives solutions and $W(x)$ has a peak on ABM.

Fig. 3 shows $W(x)$ which describes the qualitative amplitude distribution defined by Eq. (17). $W(x)$ in the air environment of Fig. 3(a) shows a clear peak at each frequency, where the peak indicates the resonance at the local place. Comparing $W(x)$ at different frequencies, it is found that the peak position shifts to smaller x as the frequency increases. It is also found that the peak value of $W(x)$ decreases as the frequency increases. Fig. 3(b) shows the $W(x)$ in the liquid environment. As same with the result in the air environment, the peak position shifts to smaller x as the frequency increases. However, compared with the results in the air environment, $W(x)$ in the liquid environment shows peaks at smaller frequencies. By comparing the results at 3.5 kHz in Fig. 3(a) and (b), the effect of the surrounding fluid on $W(x)$ can be discussed in detail. Although ABM is vibrated at the same frequency, it is found that the peak position in the liquid environment is shifted to smaller x and the form of $W(x)$ is moderated compared with those in the air environment. These results indicate that the stronger fluid-structure interaction due to the higher density decreases the resonant frequency and relaxes the resonance. Based on Eq. (16), the mechanism of decreasing the resonant frequency in the liquid environment is that the effective mass for the vibration is increased due to the much higher density of the liquid compared with that of the air. The reason for the moderated resonance is discussed later.

Fig. 4(a) shows the distributions of $k(x)$ in the air environment at 3.5, 6.0, 9.0, and 12.0 kHz. In Fig. 4(a), it is found that $k(x)$ in the air environment increases with x. There is a certain position of x_{inc} where $k(x)$ rapidly increases. x_{inc} is mathematically defined as the position where $k(x)$ gives the largest gradient. At larger x than x_{inc}, $O(k(x))$ is 10^2–10^3 m^{-1} and the wavelength is 63–6.3 mm. At smaller x than x_{inc}, $k(x)$ is very small which corresponds to the extremely long wavelength. Comparing the results at different frequencies, it is found that x_{inc} becomes smaller at the higher frequency. It is also found that x_{inc} is close to the peak position of $W(x)$ in Fig. 3(a). Since the result is obtained by the analysis based on the WKB solution, the wavelength should be short enough to treat $b(x)$ as a slowly varying function. Furthermore, $k(x)$ should be gradually changed by x. Thus, the precision of result should be relatively bad around x_{inc} and at smaller x than x_{inc}. Fig. 4(b) shows the $k(x)$ distributions in the liquid environment at 1.0, 2.0, 3.0, and 3.5 kHz. $k(x)$ in the liquid environment gradually increases with x compared with that in the air environment. Although the resonant frequencies are different between in the air and in the liquid envi-

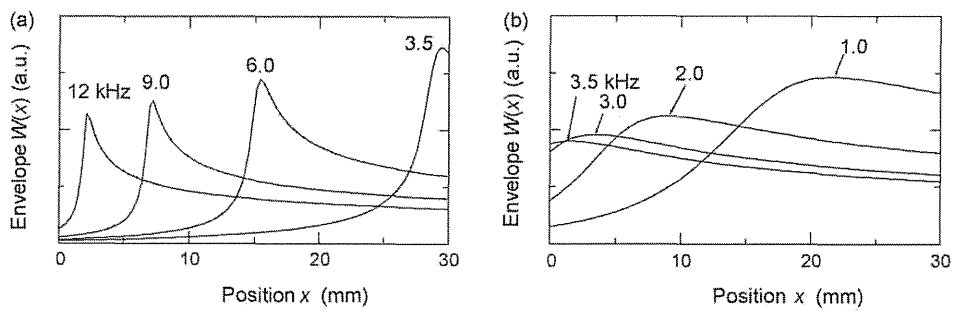

Fig. 3. Theoretical results of envelope function $W(x)$ in (a) air and in (b) liquid environments for various frequencies.

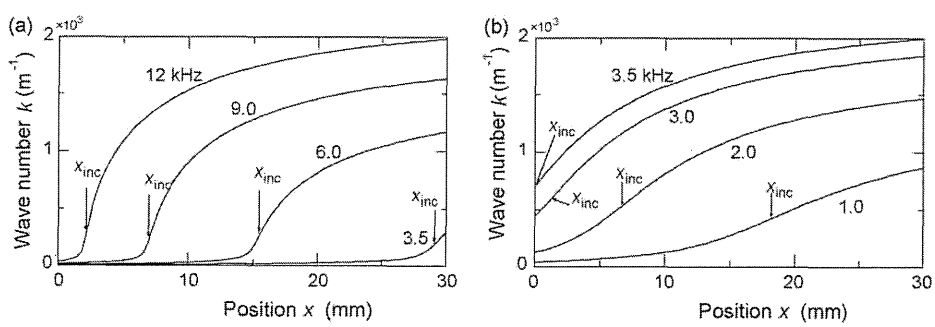

Fig. 4. Theoretical results of wave number $k(x)$ in (a) air and in (b) liquid environments for various frequencies.

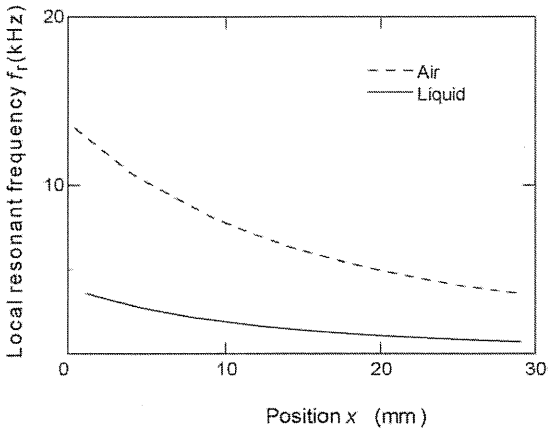

Fig. 5. Theoretical results of local resonant frequencies in air and in liquid environments.

ronments, the orders of $k(x)$ around x_{inc} and at larger x than x_{inc} are similar to the results in the air environment. From this result, it can be said that the resonance is governed by the wavelength which is strongly related to the geometry of ABM. x_{inc} is closely connected with the peak position of $W(x)$ shown in Fig. 3(b). Furthermore, the reason for the moderated resonance in the liquid environment can be explained by comparing Fig. 4(a) and (b). Since $k(x)$ in the air environment rapidly changes around the resonance place as shown in Fig. 4(a), the evolution of $W(x)$ also does. It is owing to the fact that the resonance condition is governed by the wavelength. On the contrary, since $k(x)$ in the liquid environment gradually changes around the resonance place as shown in Fig. 4(b), the peak of $W(x)$ becomes to be moderated.

Fig. 5 shows the relationship between the resonant frequency f_r and x. Both f_r in the air and in the liquid environments decrease as x increases and f_r in the liquid environment is lower than that in the air environment due to the increase of effective mass. Although the auditory frequency is widely ranged from 20×10^{-3} to 20 kHz, the device can cover only the part of it. It works at the frequencies over the ranges of 3.5–14 kHz in the air environment and 0.7–3.6 kHz in the liquid environment, respectively. For the clinical application, the device should be optimized to realize the frequency selectivity in the required frequency range for a daily conversation. Furthermore, distribution of f_r should be fitted to that in the biological system from the viewpoint of natural hearing. To solve these problems, the geometrical optimizations of ABM can be effectively carried out in our future work based on the theoretical analysis developed here.

The theoretical analysis is carried out based on the experimental condition, where only the bottom side of ABM faces to the liquid. In case of ABM facing to the liquid at both sides, the difference is found in the last term of Eq. (16) which includes the effect of surrounding fluid. In case of the same fluid channel is placed on the upper side of ABM and is filled with the same liquid, the last term is double of that in Eq. (16). Consequently, the larger effect of surrounding fluid is induced, that is, the further decrease of resonant frequency is found due to the increase of effective mass for the vibration, where the figure is omitted.

Furthermore, the theoretical analysis is carried out based on the assumption of the small amplitude. The basic equations are solved by WKB treatment which cannot quantitatively predict the vibrating amplitude. Therefore, it is difficult to precisely estimate the piezoelectric output which is determined by the strain in the membrane. The investigation on the piezoelectric output can be made by the numerical analysis based on the finite element method, which is our future research.

3. Results and discussion

3.1. Performance test in air environment

The basic vibrating characteristics of ABM in the air environment are investigated as a preliminary experiment. This experiment is conducted without filling the fluid channel with the silicone oil. The amplitude distributions of vibration are measured by applying acoustic waves of 75 dBSPL. The frequency is controlled over the range of 1.0–20.0 kHz, which covers the part of human's audible frequency. The amplitude of vibration becomes relatively small at the frequencies both lower than 3.0 kHz and higher than 18.0 kHz. It may be owing to that ABM is designed to have LRF for the first mode over the range of 3.5–14.0 kHz in the air environment. Fig. 6(a)–(d) show the amplitude distribution at f = 4.0, 6.0, 9.0, and 12.0 kHz, respectively. The amplitude distribution clearly shows dependence on the frequency. The place with maximum amplitude, where ABM is locally resonating, shifts to the smaller x as the frequency increases. This relationship between the position of resonating place and the frequency successfully has similarities with that of biological basilar membranes. Furthermore, in Fig. 6(c) and (d), it is found that there are several extrema indicated by arrows at the larger x than that of resonating place. These may be induced by the standing wave due to the traveling waves to positive and negative directions of x. The reason why the standing wave is not observed at the smaller x than that of resonating place is that the wavelength is relatively long at those positions. This is confirmed by the theoretical result of relatively small $k(x)$ as shown in Fig. 4(a). In the biological cochlea, the acoustic wave travels from the basal to the apex. However, in our experiment, it is applied to the entire ABM from the air. As a result, the relatively large effects of the standing waves are induced in our experiment due to the small damping effects from the surrounding fluid.

Fig. 7(a)–(c) show the frequency dependences of vibration and the piezoelectric output at Ch. 6, Ch. 12 and Ch. 18, respectively. The amplitudes of vibration and the piezoelectric output are plotted by a solid line and by a broken line, respectively. It seems that each electrode has a specific frequency where the electrode gives

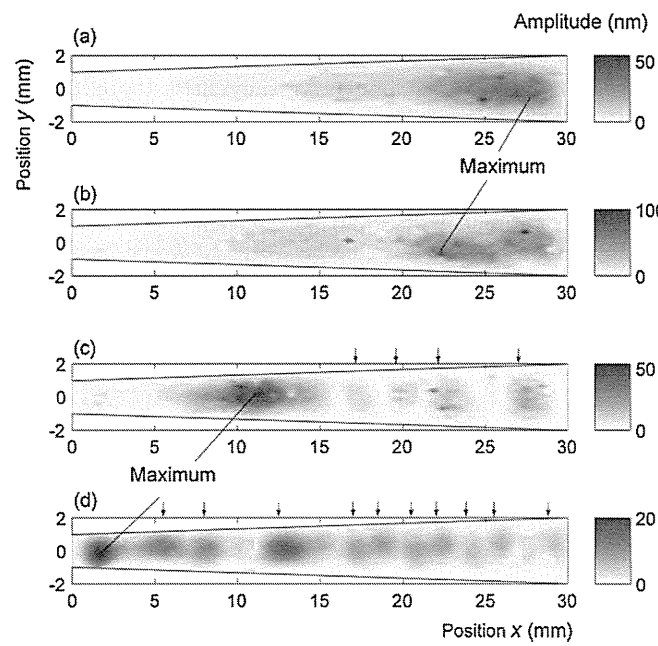

Fig. 6. Experimental results of contour maps of vibration amplitude at (a) f = 4.0 kHz, (b) 6.0 kHz, (c) 9.0 kHz, and (d) 12.0 kHz in air.

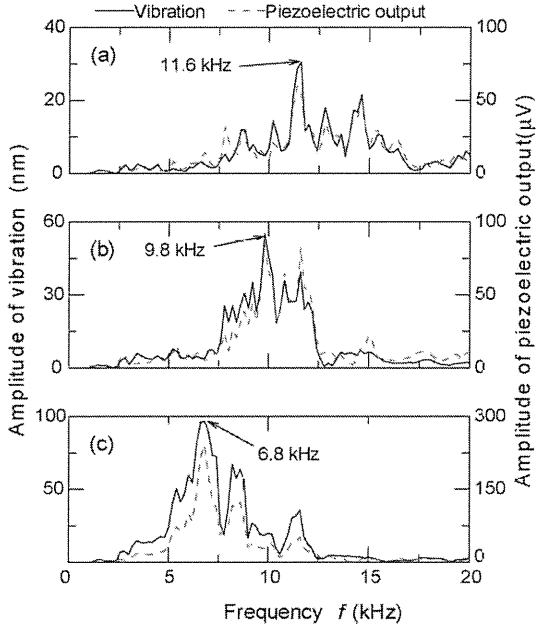

Fig. 7. Experimental results of vibration amplitude and piezoelectric output from (a) Ch. 6, (b) Ch. 12 and (c) Ch. 18 at various frequencies in air.

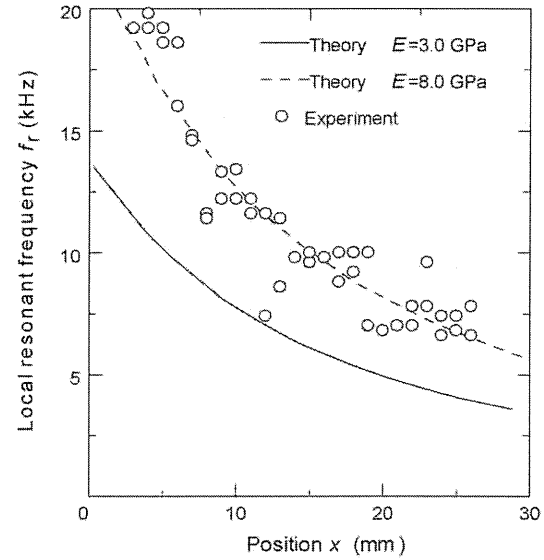

Fig. 8. Comparison of theoretically and experimentally obtained results of local resonant frequency f_r in air.

relatively large outputs. The specific frequency is defined as LRF of electrode. LRF decreases as the channel number increases, i.e., as the position x increases. Extremal amplitudes at other frequencies of LRF may indicate the effect of standing waves. That is, in case of the electrode locates on the antinode of standing wave, the amplitude from the electrode increases. On the other hand, in case of the electrode locates on the node, the amplitude decreases. As reported in Refs. [7,8,17], pretension in the membrane may be a main reason for the standing wave which results in the multiple-peaks as shown in Fig. 7. However, it is difficult to precisely control the pretension in our fabrication process. Therefore, the mechanism of this result remained to be solved in this study. The frequency dependences of vibration and the piezoelectric output are qualitatively similar to each other. The reason of their similarity can be explained as follows. Since ABM is relatively narrow in y direction compared with that in the x direction, the vibration is mainly effected by the boundary conditions at $y = \pm b(x)/2$. As the result of that, the piezoelectric output is dominated by the ABM's local structural strain in y direction. Furthermore, the piezoelectric constant in y direction is larger than that in x direction. This may make the strong dependence of piezoelectric output on the strain in y direction.

Fig. 8 shows the relationship between LRF f_r and position x. Circles are LRF which are determined by the vibration and the piezoelectric output. LRF decreases from 19.8 to 6.6 kHz as x increases. This experimental LRF is in qualitative agreement with the theoretical prediction of Eq. (16) which is drawn by the solid line. In the quantitative comparison, however, almost all experimental results are slightly higher than the predictions. One of possible reasons is the underestimation of E. Since E from literatures widely distributes as 3.0–11.0 GPa [18,19], we used a reference value of 3.0 GPa for the prediction. If we use higher value of 8.0 GPa, the precision is improved as shown by the broken line in Fig. 8.

Fig. 9(a) shows the relationship between the external sound pressure and the amplitude of vibration in ABM. This investigation is conducted at LRF of each electrode. To show the results over the range of 60–90 dBSPL, those are drawn in the log-dBSPL plot. From the gradient of results, it is found that the amplitude of vibration at LRF linearly increases with the sound pressure. The amplitude increases with the channel number, that is, with ABM's width. Fig. 9(b) shows the relationship between the sound pressure and the amplitude of piezoelectric output. The amplitude of piezoelectric output also shows the linear relationship with the sound pressure. These results suggest that the device can detect not only the frequency of acoustic wave but also the magnitude of it.

3.2. Performance test in liquid environment

The performance of device in the liquid environment is investigated by filling the fluid channel with the silicone oil with the

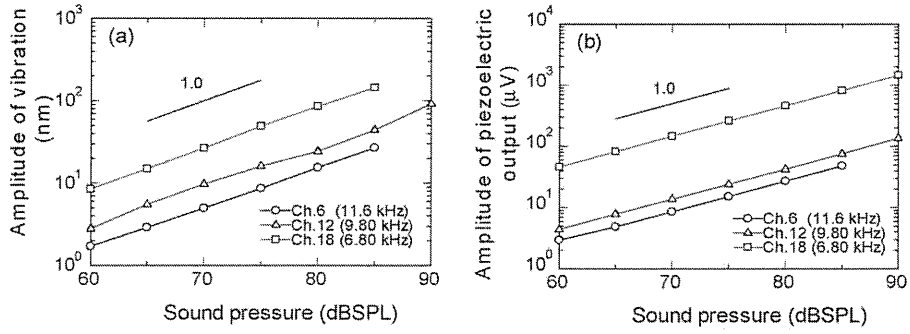

Fig. 9. Experimental results in effect of sound pressure on amplitudes (a) of vibration and (b) of piezoelectric output in air.

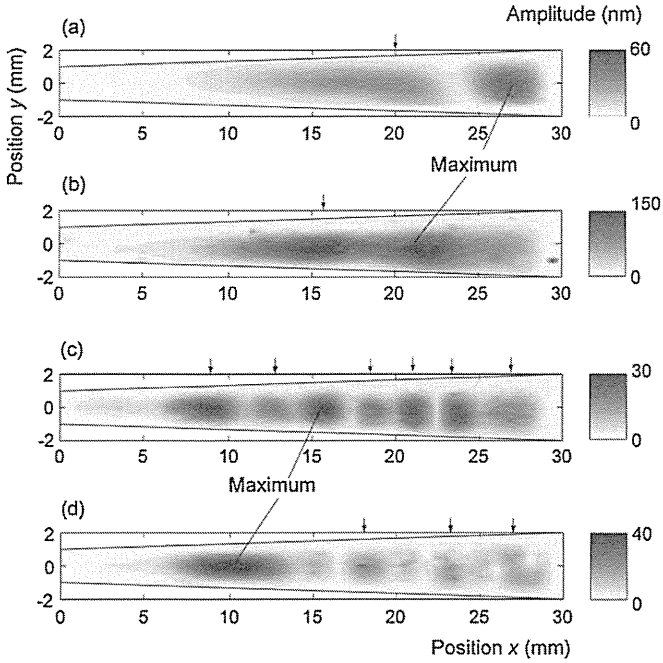

Fig. 10. Experimental results of contour maps of vibration amplitude at (a) f = 1.5 kHz, (b) 2.0 kHz, (c) 3.0 kHz and (d) 4.0 kHz in silicone oil of 1.75×10^{-3} Pa s.

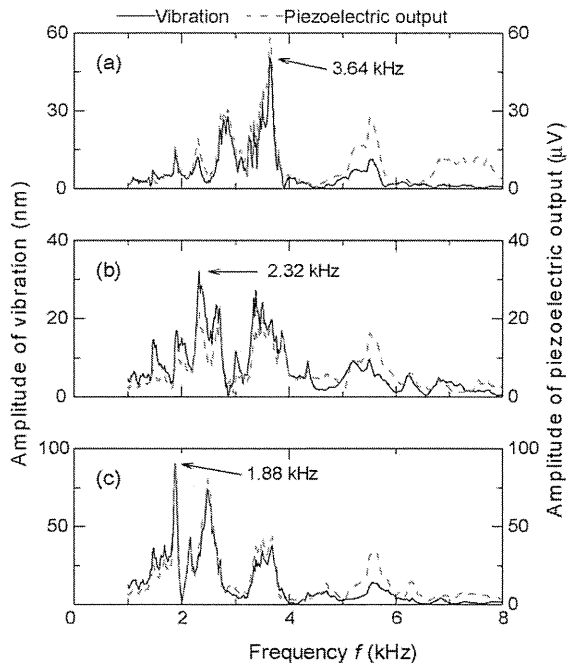

Fig. 11. Experimental results of vibration amplitude and piezoelectric output from (a) Ch. 6, (b) Ch. 12 and (c) Ch. 18 at various frequencies in silicone oil of 1.75×10^{-3} Pa s.

viscosity of 1.75×10^{-3} Pa s. This investigation is intended to test the applicability of device for implanting into the cochlea. Since the outputs from ABM are relatively small compared with that in the air environment, the sound pressure is increased to be 85 dBSPL for this experiment. This decrease of outputs in the silicone oil may be caused by energy dissipation in liquid environment due to the viscosity and the stronger fluid-structure interaction of ABM due to the density, however, the detailed mechanism has not been clarified. Fig. 10 shows the contour maps of amplitude distribution at (a)f = 1.5 kHz, (b)2.0 kHz, (c)3.0 kHz and (d) 4.0 kHz, respectively. The qualitative frequency dependence of vibration is similar to that in the air environment. That is, the location with the maximum amplitude is shifted to the smaller x as the frequency increases. However, the frequency ranges where ABM shows peak amplitude in the silicone oil are lower than that in the air environment. Comparing Fig. 6(a) and Fig. 10(d), the effect of surrounding fluid can be discussed in detail. In spite of driving the device at the same frequency of 4.0 kHz, these results clearly show the different vibration behavior. It is found that the maximum amplitude is found at the smaller x in the silicone oil compared with that in the air environment. This difference may be caused by the fluid-structure interaction as discussed in the earlier section. That is, compared with the result in the air environment, the effective mass for the vibration is increased in the silicone oil. As a result, the place with maximum amplitude is shifted to the smaller x in the silicone oil at the same frequency. Furthermore, the effects of standing wave in the silicone oil which are indicated by arrows seem relatively large compared with that in the air environment. This fact is predicted by the theoretical analysis that the resonance is relaxed due to the surrounding liquid as shown in Fig. 3.

Fig. 11 shows the frequency dependences of vibration and piezoelectric output, where they are indicated by a solid line and the broken one, respectively. As same with those in the air environment, the two amplitudes show the similar tendency to each other. The amplitudes have peaks at each specific frequency which is also described as LRF for convenience. LRF of Ch. 6, Ch. 12, and Ch. 18 are obtained as 3.64, 2.32, and 1.88 kHz, respectively. From Fig. 11, it is confirmed that the ABM's frequency selectivity is successfully realized even in the liquid environment. However, comparing Figs. 7 and 11, the peak height at the LRF becomes low, i.e., the selectivity seems worse than that in the air environment. This result qualitatively agrees with the theoretical result that the peak is relaxed in the liquid environment as shown in Fig. 3. In order to dramatically improve the frequency selectivity, it is expected that the sensor including the active feedback control which mimics the biological cochlea should be developed in future.

Fig. 12 shows the relationship between f_r and x in the silicone oil. From Fig. 12, it is found that the LRF decreases from 4.9 to 1.4 kHz as x increases, where the range is lower than that in the air environment. The experimentally obtained LRF is compared

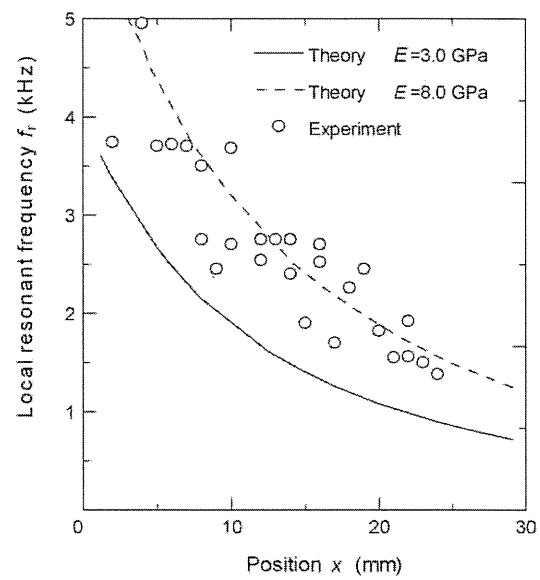

Fig. 12. Comparison of theoretically and experimentally obtained results of local resonant frequency f_r in silicon oil of 1.75×10^{-3} Pa s.